Article

Differential cross sections and analysing powers for PP -> $\pi^-\pi^+$ and K̄K⁺ from 360 to 1550 MeV/c

HASAN, A., *et al*.

Reference

UNIVERSITÉ
DE GENÈVE

Differential cross sections and analysing powers for $\overline{P}P \to \pi^-\pi^+$ and K^-K^+ from 360 to 1550 MeV/c

A. Hasan, D.V. Bugg, J.R. Hall [1] and R.L. Shypit [2]

Queen Mary and Westfield College, London E1 4NS, UK

F. Tessarotto, R. Birsa, F. Bradamante, S. Dalla Torre-Colautti, A. Martin,
A. Penzo, P. Schiavon and A. Villari [†]

INFN Trieste and University of Trieste, Trieste, Italy

S. Degli-Agosti, E. Heer, C. Lechanoine-Leluc, Y. Onel [3] and D. Rapin

DPNC, University of Geneva, Geneva, Switzerland

R. Kunne [4], K. Bos, J.C. Kluyver [†] and L. Linssen [5]

NIKHEF-H, Amsterdam, The Netherlands

A.S. Clough

University of Surrey, Guildford, Surrey, UK

Analysing powers and differential cross sections for $\overline{p}p \to \pi^-\pi^+$ and $p\overline{p} \to K^-K^+$ have been measured over the full angular range using a polarised target at LEAR at 20 beam momenta from 360 to 1550 MeV/c. Discrepancies in the normalisation of earlier dσ/dΩ data at low momenta are clarified. Above 1000 MeV/c, A_{0N} results confirm values close to +1 over most of the angular range for both reactions, in excellent agreement with earlier data of lower statistics. Below 1000 MeV/c, where the analysing power is measured for the first time, large variations of A_{0N} with energy and angle are present.

1. Introduction

The high quality $\overline{p}$-beams available at LEAR allows detailed meson spectroscopy in the mass range above 1900 MeV/c^2. Here we report data on the

---

[1] Present address: BNL, Upton, NY 11973, USA.
[2] Present address: University of British Columbia, Vancouver, BC V6T 2A6, Canada.
[3] Present address: University of Iowa, Iowa City, IA 52240, USA.
[4] Present address: LNS, F-91191 Gif-sur-Yvette, France.
[5] Present address: CERN, CH-1211 Geneva 23, Switzerland.
[†] Deceased.

two-body channels $\bar{p}p \rightarrow \pi^-\pi^+$ and K^-K^+ at 20 momenta from 360 to 1550 MeV/c. Differential cross sections and analysing powers were measured simultaneously using a polarised target. Statistically, the results are a significant improvement on earlier data. The A_{0N} data explore for the first time the momentum range below 1000 MeV/c.

For $\bar{p}p \rightarrow \pi^-\pi^+$, parity, charge conjugation and isospin invariance lead to the constraint that isospin I is zero for even angular momentum (L) in the final state; $I = 1$ for L odd. As in the crossed channel $\pi^+p \rightarrow \pi^+p$, there are, therefore, only two amplitudes. There is a reasonable hope that data on both $d\sigma/d\Omega$ and A_{0N}, together with constraints from analyticity, will lead to a unique set of amplitudes or at worst a limited number of ambiguities. In the helicity basis, the amplitude may be written F_{++} and F_{+-}, where

$$\frac{d\sigma}{d\Omega} = \tfrac{1}{2}\bigl(|F_{++}|^2 + |F_{+-}|^2\bigr),$$

$$A_{0N}\frac{d\sigma}{d\Omega} = \mathrm{Im}\bigl(F_{++}F_{+-}^*\bigr).$$

Data on $d\sigma/d\Omega(\bar{p}p \rightarrow \pi^0\pi^0)$ are valuable, particularly in eliminating discrete ambiguities. For $\bar{p}p \rightarrow K^-K^+$, the restriction on isospin is absent, so there are four spin–isospin combinations; hence, without data on $\bar{p}p \rightarrow \overline{K}^0K^0$ a full amplitude analysis is not possible.

There have been several earlier measurements in the momentum range up to 2500 MeV/c. The earliest systematic measurements of differential cross sections, from 700 to 1100 MeV/c, were made by Mandelkern et al. [1]; their paper gives references to earlier scattered bubble chamber data. The first asymmetry measurement for $\bar{p}p \rightarrow \pi^-\pi^+$ was performed at BNL [2] based on 350 events collected at 1640 MeV/c. A major step forward was taken by Eisenhandler et al. [3], who reported differential cross sections at 20 momenta from 790 to 2430 MeV/c; they used spark chambers and a liquid hydrogen target at the CERN PS. The same group later used a polarised target to measure polarisations and differential cross sections at 11 momenta from 1000 to 2200 MeV/c [4] with good angular coverage for both the $\pi^-\pi^+$ and K^-K^+ final states. An amplitude analysis [5] of the $\pi^-\pi^+$ data revealed evidence for three resonances in the $\pi^-\pi^+$ channel with spins 3, 4 and 5 in the mass region 2020–2580 MeV/c². Later analyses added $\bar{p}p \rightarrow \pi^0\pi^0$ differential-cross-section measurements of Dulude et al. [6] from 1100 to 2000 MeV/c and reached somewhat different conclusions on the content of resonances [7–9]. Whatever the resonances, both angular distributions and polarisations show a remarkably systematic t-dependence which varies slowly and smoothly with energy, suggesting an underlying coherence amongst partial wave amplitudes [10].

In the last decade, differential-cross-section data have appeared at lower momenta. These data have been summarised by Tanimori et al. [11], who reported

differential cross sections folded about 90° at 15 momenta from 360 to 760 MeV/c. They did not confirm a peak at 490 MeV/c observed in an earlier measurement of the unfolded $\bar{p}p \to K^- K^+$ differential cross section [12]. It is important to be aware that the second paper [11] of Tanimori et al. recommended substantial renormalisations of the first set of results [12]. The second set agree with data of Sai et al. [13], measured with a liquid-hydrogen bubble chamber from 403 to 728 MeV/c. Recently, Bardin et al. [14] have reported measurements for the pion channel at extremely low momenta, 158–275 MeV/c.

It is not our intention here to compare data with theoretical models. References to many such model calculations are given in ref. [11].

There are two specific motivations for the present experiment, apart from the obvious improvement in statistics. The first is to extend polarisation measurements below 1 GeV/c, where there were no previous data. The second is to explore in small steps of momentum the range 1400 to 1500 MeV/c, where the Mark III collaboration [15] has reported an unusually narrow state $\xi(2230)$ decaying to both $K^- K^+$ and $\bar{K}_S^0 K_S^0$. If it were to couple to $\bar{p}p$, its width would be magnified in terms of $\bar{p}$-momenta around 1425 MeV/c, because of kinematics. Sculli et al. [16] have searched the momentum range 1250–1560 MeV/c, but find no structure in the ratio of $\pi^- \pi^+$ to $K^- K^+$ events over the angular range $|\cos \theta| < 0.5$. A more subtle way of looking for it is via interference with other states in $d\sigma/d\Omega$ and particularly in A_{0N}, which is phase sensitive. We do not see narrow structure, but we do find a rapid rise in the Legendre coefficients b_4 to b_6 fitting $A_{0N} \, d\sigma/d\Omega$ in $\bar{p}p \to K^- K^+$ above 1200 MeV/c. The interpretation of this result will be discussed in the conclusions.

The paper is organised as follows. Sect. 2 describes the experimental set-up and sect. 3 the separation of $\bar{p}p \to \pi^- \pi^+$ and $K^- K^-$ signals from each other and from background processes. Sect. 4 presents the results and an analysis of angular distributions of both $d\sigma/d\Omega$ and A_{0N} in terms of Legendre series. An amplitude analysis is in progress and will be reported separately. A preliminary account of asymmetry results has been given earlier [17]. The data were taken with the same equipment and at the same time as data on $\bar{p}p$ elastic scattering; these data have been published by Kunne et al. [18].

2. Experimental apparatus

The experiment was done at LEAR using a $\bar{p}$-beam with an intensity typically $4 \times 10^5 \, s^{-1}$. The layout of the equipment is shown schematically in fig. 1. It was designed to provide full angular coverage for the two-body reactions. The $\bar{p}$-beam was defined by scintillation counters and MWPCs before the target, which was located between the polepieces of a 2.5 T magnet. The outgoing particles of an event were measured by cylindrical MWPCs surrounding the target region; ho-
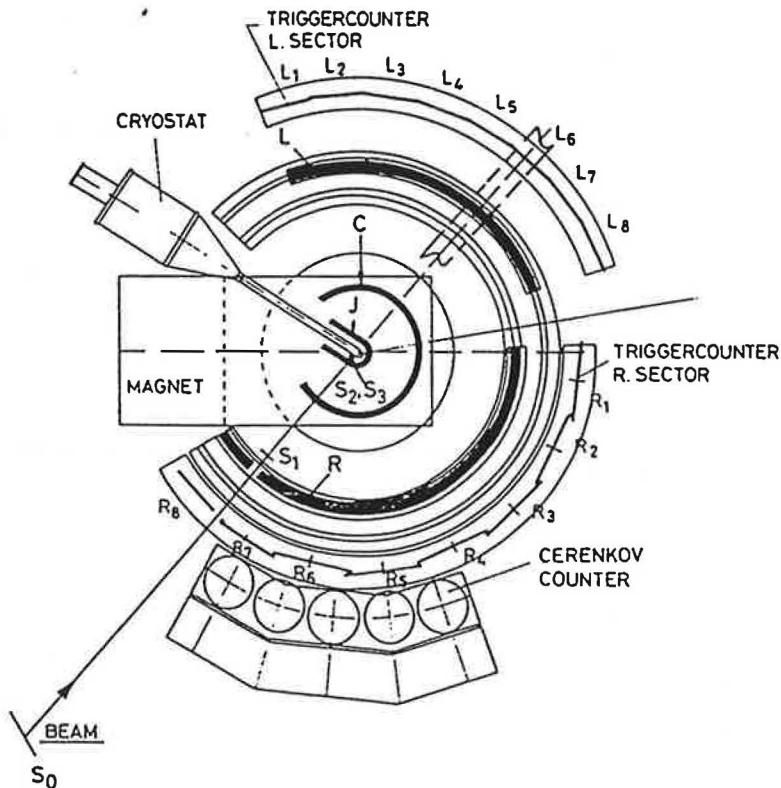
Fig. 1. A plan view of the experiment from above.

doscope counters triggered the data acquisition system. Non-interacting $\bar{p}$ were deflected by the magnet of the polarised target and emerged through the gap between the outermost layer of chambers and hodoscope counters. Background from multimeson annihilations was reduced by veto counters covering the pole faces of the magnet.

2.1. THE POLARISED TARGET

The intense and homogeneous magnetic field needed by the polarised target was provided by a CERN C-shaped magnet (MEP-12) with pole faces of 17 cm diameter and a gap of 6.4 cm. The field value at the centre was measured by NMR techniques to be 2.501 T, with a uniformity over the target region of $\pm 0.01\%$. A complete map of the field, obtained with Hall probes, was parametrised and used in the reconstruction programs.

The target itself was a 3.0 cm long cylinder, parallel to the beam, with a diameter of 1 cm. It was placed in a dilution ^{3}He$-^4$He refrigerator operating at

0.5 K. The target was filled with pentanol beads ($C_5H_{11}OH + 5\%$ residual H_2O) and was doped with CrV complexes. The target thickness was 1.94 g/cm^2, with a hydrogen thickness of 0.264 g/cm^2. The polarisation of free protons was dynamically induced (via coupling to the CrV electrons) by microwave power at two frequencies close to 90 MHz, supplied from a carcinotron oscillator. It reached typical values of $+72\%$ and -77% and was measured each second by an NMR system with $\pm 0.5\%$ reproducibility and good linearity.

Polarisation reversal was done by changing the microwave frequency and took typically 30 min. Absolute calibrations were made at the beginning and end of each running period with an estimated accuracy of $\pm 4\%$. The accuracy of this calibration governs the normalisation uncertainty of A_{0N} results, but the shape of A_{0N} dσ/dΩ is independent of normalisation.

Background from protons bound in nuclei was measured with a dummy target at three momenta: 523, 1089 and 1434 MeV/c. In these runs, the target contained teflon $(CF_2)_n$ wires, chosen so that the energy loss was the same as in the pentanol target. In absolute magnitude the background varies rather little with angle and increases steadily with decreasing momentum, roughly in line with the $\bar{p}p$ total cross section. This background may be attributed partly to two-body events from nuclei and partly to many-body annihilation. For other momenta between 523 and 1434 MeV/c the shape of the background versus χ^2 is interpolated linearly between the three momenta given above; outside these momenta, it is taken from dummy data at 523 or 1434 MeV/c. The magnitude of the background is normalised to the tail of the χ^2 distribution for fitted events. This is discussed in sect. 3.

Momenta are known with an accuracy of ± 1 MeV/c from settings of LEAR. The momentum spread of the beam over the target varied from ± 2.2 MeV/c at the highest momenta to ± 22.5 MeV/c at the lowest; values at the entrance and exit of the target are quoted for low momenta in table 1.

There is a systematic error of about $\pm 5\%$ in measuring the packing density of the target. This density varied slightly from run to run, leading to the suspicion that the target did not fill in a fully homogeneous way. The combined uncertainty in target density is estimated to be $\pm 10\%$ and there is a consequent normalisation uncertainty in differential cross sections of this amount, common to all angles.

TABLE 1

Central momenta (MeV/c) and those at entrance and exit of the polarised target

Central	Entrance	Exit
360	381	336
404	420	385
467	479	455
497	509	486

2.2. THE BEAM

The beam was defined by a coincidence between counters S0 (at the first focus 24 m upstream), S1 and (S2 ⊕ S3). Counter S2 was 1 cm in diameter and 1 mm thick. It was used to record data for asymmetry measurements. Counter S3, 0.5 mm thick and 23 mm upstream of the centre of the target, was 0.7 cm in diameter, with the intention that a beam passing through it would traverse the entire length of the target without multiple scattering out through the sides. S3 was used to record data for differential-cross-section measurements simultaneously with polarisation data triggered by S2.

A small steering magnet 4 m before the target compensated the bending of the beam by the magnet of the polarised target. At the higher momenta, the beam spot measured typically 1 mm horizontally by 3 mm vertically and was confined well within the dimensions of the polarised target. Below 1 GeV/c, multiple scattering in material upstream increased the spot size until, at the lowest momenta, it more than filled S3. At the lowest four momenta there is some tentative evidence for loss of beam down the length of the target due to multiple scattering; the normalisations at these lowest momenta should consequently be regarded as less reliable than those of the higher momenta. Shapes of the angular distributions are unaffected, as are the ratios of K^-K^+ and $\pi^-\pi^+$ differential cross sections.

2.3. MWPCs

At each momentum, the beam focus was observed using small multiwire chambers, B1 and B2, 1.3 m upstream of the target. The focus was then moved to the target centre by calculation. These beam chambers were flat MWPCs having one plane of vertical and one plane of horizontal wires, each with 1 mm pitch and an active area of 95×95 mm^2. Each chamber had three 10 μm Al cathodes and two windows made of 50 μm thick mylar to minimise multiple scattering.

The beam was scanned vertically and horizontally across the target and centred by optimising the transmission, as monitored by a counter downstream of the target in coincidence with S0 · S1. Counters S2 and S3 were centred horizontally using a traversing table and allowing for the bending of the beam by the magnetic field of the polarised target. The polarised target itself could be rotated inside the cryostat in three angular steps of 5°, so as to keep it approximately parallel to the beam direction.

Immediately around the nose of the cryostat, between the polepieces of the polarised target, a J-shaped MWPC (J) provided coordinates as close as possible to the vertex of the interaction. The spine and walls of the chamber were made from low-density polystyrene foam, so as to minimise multiple scattering. For high efficiency, it had two planes of vertical sense wires of 1 mm pitch. The cryostat had a diameter of 42 mm and the wire planes had a minimum distance from the centre

of the target of 32 and 52 mm and a vertical active region of 30 mm. The outer plane was equipped with cathode readout from 6 mm wide copper strips; these strips were separated by 2 mm gaps and were at an angle of 30° to the horizontal plane.

A cylindrical MWPC (C), mechanically similar to the J-chamber, was placed at the optimum position for momentum measurements. Two planes of vertical wires with 1.25 mm spacing were put at radii of 21 and 23.5 cm from the target. The C-chamber covered a lab angular range of 261° and had an active region 11.0 cm high.

Particles scattering to the left of the beam crossed a third cylindrical chamber (L) outside the magnetic field. Two horizontal and two vertical coordinates were provided by this chamber, which covered a polar angle of 91.5° and an azimuthal angle from $-14°$ to $+14°$. The two planes of vertical wires were at 67.2 and 70.4 cm from the centre of the target and the wire pitch was 3 mm; the cathodes were at 6.0 mm from the wires. The chamber walls were made from an expanded polyurethane foam. Copper cathode strips, 6 mm wide separated by 2 mm gaps and inclined at $\pm 13°$ to the horizontal, provided vertical coordinates with an accuracy of ± 0.6 mm.

At the right of the beam a similar but larger chamber (R) was placed. The two wires planes were at 57.2 and 60.4 cm from the target and the wire pitch was 3 mm. Two carbon fibre poles in the central spine of this chamber supported the tension of the wires. The beam entered through a small hole, 77 mm horizontally $\times 36$ mm vertically; the small loss of geometrical coverage due to this hole was easily accomodated in evaluating differential cross sections.

Two different R-chambers were used, one for momenta above 600 MeV/c and covering an arc of 170°; a second, slightly smaller one, covering an arc of 150°, was used at lower momenta. This allowed coverage of the maximum angular range without the exit beam hitting the frame of the chamber. The result of this geometry was that the complete angular range was covered, either to left or right, at all momenta.

We shall denote the centre of mass scattering angle by θ and the azimuthal angle by ϕ. The L-chamber covered angles up to about $\theta = 102°$ for pions and 107° for kaons. The R-chamber covered angles to $\theta = 180°$. There was some overlap near $\theta = 90°$ c.m. between events collected to both left and right.

All chambers achieved a reconstruction accuracy of $\sim 30\%$ of wire spacings, and, ultimately, errors from multiple scattering and measurement errors were similar.

2.4. HODOSCOPE COUNTERS AND TRIGGER

Events were triggered by a coincidence between the beam and one of the eight hodoscope counters HL to the left and the appropriate HR counters to the right.

HL counters were 35 cm high × 29 cm wide at 95 cm from the target. Nine HR counters, 42 cm high × 21 cm were at 81 cm radius. Counters HR7 and HR8 had a hole for the incoming beam. When the smaller R-chamber was in use, one less HR counter was used.

Both L- and R-chambers and all hodoscope counters could be rotated into the beam for setting-up purposes. This allowed precise setting up and measurement of efficiencies. Hodoscope counters had efficiencies > 99.8% for relativistic particles. Chamber efficiencies were > 98% for relativistic particles. In view of the two planes in each chamber, overall efficiencies of J, C, L and R were > 99% and losses due to their inefficiencies were negligible.

Behind the upstream part of the R-chamber were five Cerenkov counters. The intention was to check π-K separation. These Cerenkov counters achieved 90% efficiency with 10% crosstalk between π and K; however, the separation of $\pi\pi$ from $\overline{K}K$ on the basis of kinematics was actually superior to that of the Cerenkov counters, so the latter ultimately played no role in the analysis.

The signals from all scintillation counters were fed to three LeCroy ECL programmable logic units to form the pretrigger coincidence $P = B \cdot \bar{V} \cdot L \cdot R \cdot \overline{\text{Busy}}$, where B is the beam signal, V is the pole face veto $VT + VB$, L is a general OR of all HL counters, R is the OR of the HR counters. All the electronics were gated off by the Busy signal during the processing of events, so as to avoid dead-time losses. Events with more than two charged particles were vetoed.

The first selection of candidate events was made on the basis of the HR-HL multiplicity and correlation. Using the overlaps between adjacent counters to define 15 separate regions, coincidences were required from kinematically allowed combinations. Only those combinations lying within six standard deviations of multiple scattering of a two-body reaction were used to produce a first-level trigger.

A further on-line selection was made on the basis of L- and R-chamber coordinates in a way conceptually similar to the hodoscope correlation. A large table of kinematically allowed hit pairs was prepared beforehand for each momentum. Any hit in front of the HL trigger counter was combined with any hit in front of the HR trigger counter and compared with the table. If a kinematically allowed combination was within 6σ, the event was accepted.

The rejection of multipion annihilations was very efficient (98%) for events originating in the target or in the J-chamber, but not in the C-chamber; many of those events were accepted by the second-level trigger, thus increasing the dead-time of the acquisition system. To eliminate this background, a further filter trigger was implemented after the first running period. It ran on a dedicated J11 "starburst" processor (CES Geneva) and discarded all candidate events which had no hits in the C-chamber within broad "roads" running from the target to measured hits in the R-chamber.

Data were taken simultaneously for the three two-body reactions, $\pi\pi$, $\overline{K}K$ and
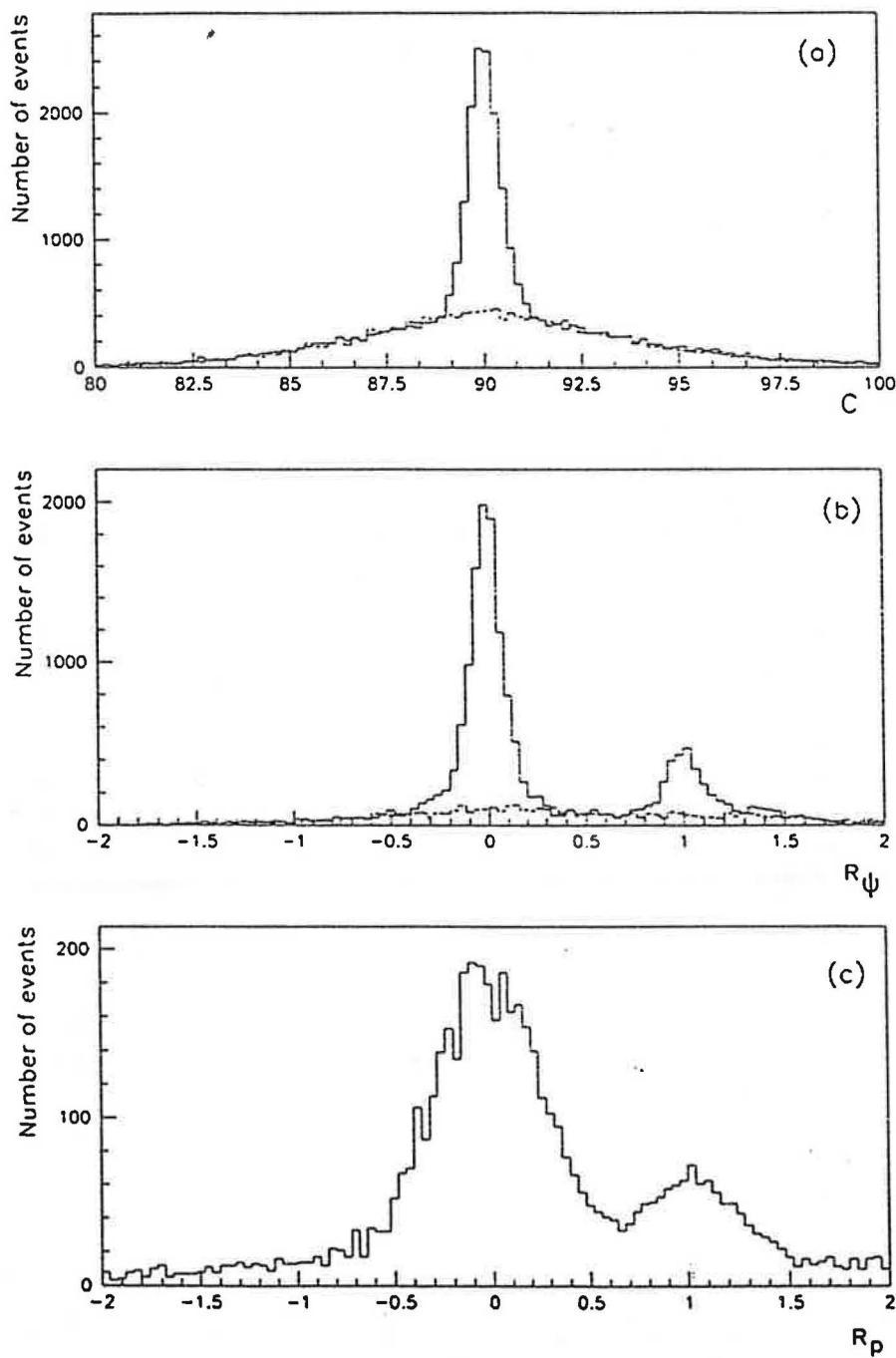
Fig. 2. (a) The coplanarity distribution, C, of candidate events for $\theta_\pi = 20°-160°$ centre of mass at 1089 MeV/c; C is measured in degrees and is 90° for coplanar events. (b) R_ψ illustrating separation of $\pi\pi$ from $\bar{K}K$ on the basis of opening angle; event selection is as in (a); R_ψ is defined so that $\pi\pi$ events are expected at 0 and $\bar{K}K$ events at 1. (c) R_p at 1089 MeV/c for $\theta_\pi = 160°-170°$ and 0°-20° centre of mass, after a coplanarity cut; $\pi\pi$ events are expected at $R_p = 0$ and $\bar{K}K$ events at 1.
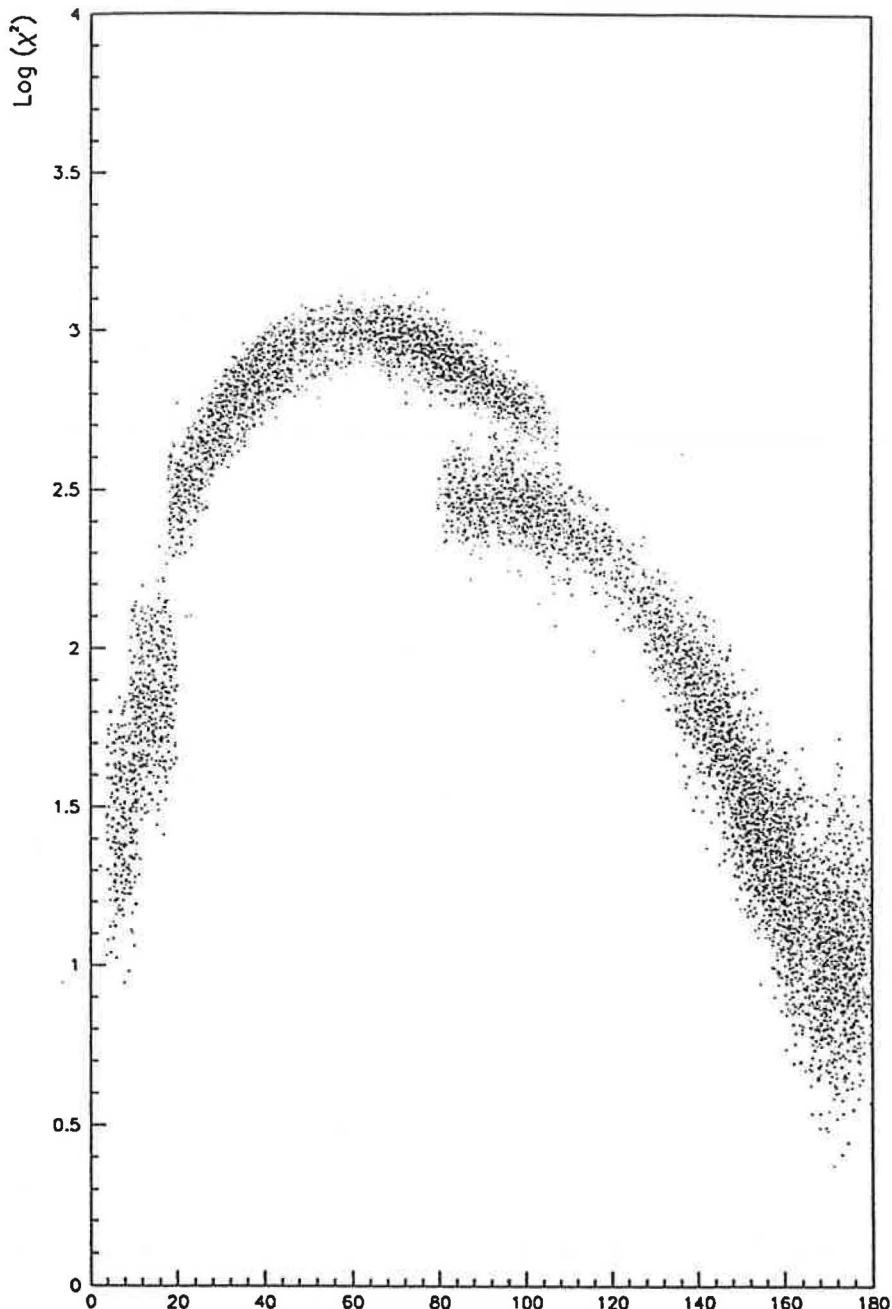
Fig. 3. Separation of $\pi\pi$ and $\overline{K}K$ events using combined coplanarity, opening angle and momenta. The plot shows $\log_{10}$ (difference in χ^2 for K^-K^+ and $\pi^-\pi^+$ hypotheses versus θ_π (degrees) at 1089 MeV/c.

$\bar{p}p$ at all momenta except below 500 MeV/c, where only the meson channels were included in the trigger. With a typical intensity of 4×10^5 $\bar{p}$/s, trigger rates were 350 Hz for the pretrigger P, 280 Hz and 120 Hz for the first- and second-level triggers, and 60 Hz for the filtered data. The readout system was CAMAC based and controlled by a PDP 11/40 computer; monitoring programs ran on two CAVIAR computers. Between May 1985 and May 1986, 42M raw events were collected on magnetic tape during 5 running periods at 20 momenta. In addition to physics data, brief runs were made at all momenta with the magnet off, in order to check chamber alignments and efficiencies.

3. Data processing

Separation of $\pi\pi$ and $\overline{K}K$ events from one another and from background depends on four kinematical quantities: (a) the coplanarity (b) the opening angle between outgoing charged tracks, (c) momenta of backward and (d) forward exit particles. Of these, coplanarity separates the majority of two-body events from multipion annihilations. An example of a coplanarity distribution is shown in fig. 2a. Next the opening angle Ψ separates $\pi\pi$ from $\overline{K}K$ cleanly over most of the angular distribution (20 to 160° centre of mass); an example is given in fig. 2b. In order to display this separation in invariant fashion, the ratio

$$ R_\psi = \frac{\Psi - \Psi(\pi\pi \text{ theory})}{\Psi(\overline{K}K \text{ theory}) - \Psi(\pi\pi \text{ theory})} $$

is plotted. For $\pi\pi$ events this peaks at 0; for $\overline{K}K$ events it peaks at 1. Finally, the momentum of the backward particle is an essential element in separating $\pi\pi$ from $\overline{K}K$ near 0° and 180° where coplanarity and opening angle become less definitive. Fig. 2c shows the separation between $\pi\pi$ and $\overline{K}K$ on the basis of momentum, after a cut on coplanarity. Quantity R_p is defined by

$$ R_p = \frac{1/p - 1/p(\pi\pi \text{ theory})}{1/p(\overline{K}K \text{ theory}) - 1/p(\pi\pi \text{ theory})}. $$

Again, R_p peaks at 0 for $\pi\pi$ events and at 1 for $\overline{K}K$. This figure shows that the momentum resolution on backward particle is typically $\pm 10\%$. With the addition of opening angle information, almost clean separation is possible between $\pi\pi$ and $\overline{K}K$ in the 0°–20° region, as demonstrated in fig. 3. Events clear of the region of overlap in fig. 2c between $\pi\pi$ and $\overline{K}K$ are used to evaluate polarisations and differential cross sections and a very small correction factor is applied to the latter to account for the overlap. The momentum of the forward particle is too high to provide more than marginal additional information.

Separation of $\pi\pi$ and $\overline{K}K$ events on fig. 3 is not clean from 170° to 180°, partially because this region is confused by beam tracks and partially because correlations between opening angle and momentum due to bending by the magnetic field make the kinematics less favourable than between 0° and 10°. However, from 0°–10° and 170°–180°, it is difficult to resolve events coming from the polarised target and those coming from S2 and S3. For this reason, we present results only from the angular region $|\cos\theta| < 0.98$, i.e. $\theta = 11°$–169°.

At an early stage in the analysis, time of flight to the trigger scintillators was examined. It was found to give at best marginal separation of $\pi\pi$ from $\overline{K}K$ and has not been used subsequently.

Processing of data goes through several stages. At the first stage, any data subject to malfunction of equipment or suspicious scaler readings are eliminated. At this stage, stability checks are made on ratios of scaler readings and also the ratios of candidate events to scaler readings. Next the ~ 1000 magnetic tapes are passed through a fast initial χ^2 fit. This fit is described in detail in refs. [19,20] and we outline it briefly here.

Suppose an event is defined by vertex coordinate v_x, v_y and v_z, polar and azimuthal scattering angles θ and ϕ, and the incident particle has vertical and horizontal inclinations α_v and α_h. Together, let us denote this event definition by a vector $p = (v_x, v_y, v_z, \theta, \phi, \alpha_v, \alpha_h)$. For such an event, coordinates in J, C, R and L chambers may be determined by tracking and expressed in terms of p:

$$x = f(p). \tag{3.1}$$

Over limited ranges of scattering angles θ, eq. (3.1) may be linearised and p is related to x by a set of matrices M:

$$x = Mp. \tag{3.2}$$

The matrices M are computed in advance and eq. (3.2) may then be inverted by the multiplication $M^{-1}x$. Using this fast process, 24 data-summary tapes are produced containing events with $\chi^2 < 4000$ for $\pi\pi$ or $\overline{K}K$ hypotheses. Subsequent refinement of these data summary tapes produces final asymmetries and differential cross sections.

3.1. FORMING MATRICES M

The detailed knowledge of equipment performance is inserted into a tracking Monte Carlo program used to produce the matrices and also tables needed for the online selection of events. The program follows generated events, solving the equations of motion in the magnetic field, including energy loss and multiple scattering, and providing coordinates at each wire plane; non-linearities of eq. (3.1) are studied by exploring the region of parameters around a grid of values of θ and

TABLE 2

Typical errors on reconstructed components of p above and below 1000 MeV/c. The z-axis is parallel to the beam, the y-axis vertical and the x-axis horizontal

Quantity	Above 1000 MeV/c	Below 1000 MeV/c
r_x (mm)	0.2–0.5	0.3–0.8
r_y (mm)	1.0–1.6	1.2–2.1
r_z (mm)	0.2–0.9	0.3–3.0
$\theta_{c.m.}$ (deg)	0.2–0.4	0.3–0.8
$\phi_{c.m.}$ (deg)	0.2–0.5	0.2–0.8
α_v (deg)	0.1–0.3	0.3–0.7
α_h (deg)	0.1–0.4	0.4–0.8

ϕ, and correction tables for eq. (3.2) are produced around each of these θ, ϕ values. Over the angular range of the equipment, the magnetic field is cylindrically symmetrical. The vertical components of magnetic field are included in the tracking procedure, hence allowing for focussing effects in the fringe field.

This tracking program is used to compute the covariance matrix of reconstructed parameters p. The accuracy varies smoothly with momentum and angle, except in extreme forward and backward directions. Typical values are given in table 2. Large correlations are present in the covariance matrix, but horizontal and vertical information is largely decoupled.

3.2. THE RECONSTRUCTION PROGRAM TREMA

The program called TREMA processes raw data and performs the following tasks on each event:

(i) Decoding and rejection of the event if the hit pattern is inadequate.

(ii) Looping over the six allowed kinematical hypotheses (elastic with $\bar{p}$ to the left, elastic with $\bar{p}$ to the right, and likewise for $\pi\pi$ and $\overline{K}K$ events). Typically, 1, 2 or 3 cases need to be considered.

(iii) Sorting of hits into tracks and filling of the hit vector x, looping over the possible combinations when more than one hit is found inside the allowed corridor.

(iv) Calculation of χ^2 for each hypothesis and rejection if $\chi^2 > 4000$; computation of p, including corrections for non-linearities in M.

(v) Discarding the event if no combination is acceptable; writing the event on a DST together with the best and second-best hypotheses. The rejection level is typically 70% and there are practically no ambiguities between elastic candidates (90% of DST events) and meson candidates.

3.3. SYSTEMATIC BIASES IN GEOMETRY

This procedure is adequate for the reconstruction of $\bar{p}p$ elastic events reported in refs. [18,19]. For $\pi\pi$ and $\overline{K}K$ events, it is apparent that the signal-to-background

ratio is not as good as it might be. There are small systematic discrepancies between coplanarity and zero, between opening angle and prediction and between momenta and predicted values. The magnitudes of these discrepancies are at the level where they can be attributed to three sources: (a) small (< 0.5 mm) misalignments of chambers, (b) slight distortions of J- and C-chambers from perfect geometry, and (c) differing drift of ionisation in pairs of gaps in the 2.5 T magnetic field. Rather than trying to unscramble these distortions, our approach has been to parametrise the discrepancies as smooth functions of angle and beam momentum. Then a new χ^2 is formed where the systematic bias is included according to

$$\chi^2 = \sum_{i=1}^{4} \left(\frac{\text{measurement}_i - \text{expectation}_i - \text{bias}_i}{\text{error}_i} \right)^2.$$

The summation is over coplanarity, opening angle, forward and backward momenta. The improvement in signal/background is illustrated in fig. 4 at 1089 MeV/c. It is particularly important in determining differential cross sections, where it is necessary to integrate the signal to large χ^2, hence including a rather large background. The χ^2 cut is applied at a fixed value, independent of θ, in order to simplify Monte Carlo evaluations of decay corrections, discussed below. For determinations of polarisation, a tighter χ^2 cut is made, as shown on figs. 5 and 6; a small amount of signal is discarded, but the overall error on A_{0N} is minimised.

In these plots, one has to beware that $\pi\pi$ events appear in the $\overline{K}K$ χ^2 plot as a broad bump away from $\chi^2 = 0$, and vice versa. To avoid this as far as possible, events fitting the $\pi\pi$ hypothesis better than that for $\overline{K}K$ and with a $\chi^2 < 40$ are eliminated from the $\overline{K}K$ plot, and vice versa.

The entire evaluation of asymmetry results has been carried out independently with (a) data summary tapes from TREMA [17], (b) data refined according to the procedure just describe [20]. Results are very close, as illustrated in fig. 7, with only a small improvement from the refinement. For $d\sigma/d\Omega$, the refinement is important. Not only does it reduce the statistical error of the background subtraction but it also reduces possible systematic errors in estimating this background.

3.4. BACKGROUND ESTIMATION

In this whole process, a major concern is the parametrisation of the background. It is determined from the shape of the χ^2 plot for events from the dummy target. Figs. 5d and 6d compare backgrounds from the dummy target at 1089 MeV/c with data from the polarised target after integrating over all angles. It is evident that there is a small but definite ($\sim 20\%$) contribution to these distributions from multipion events on hydrogen. The same effect is observed at other momenta. Also there is sometimes a discernable asymmetry for events with χ^2 above the cut-off
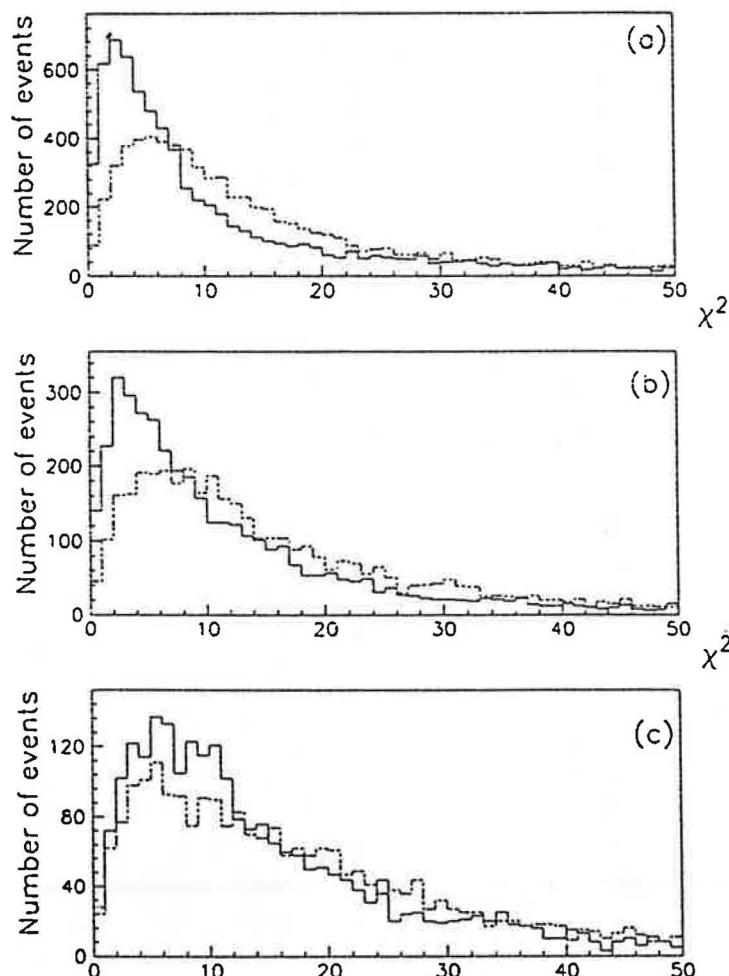
Fig. 4. Illustrating the improvement in χ^2 after allowing for systematic biases (full histogram) compared with uncorrected data (dashed histogram) at 1089 MeV/c for $\pi^-\pi^+$: (a) 0°–40° and 140°–180° centre of mass, (b) 40°–80° and 100°–140°, (c) 80°–100°.

for two-body events. We attribute this mostly to $\bar{p}p \to \pi^-\pi^+\pi^0$ from hydrogen. For this reason, the background subtraction is normalised in 20° bins of θ to the tails of the χ^2 distribution, so as to eliminate the effect of multi-pion events from hydrogen under the signal. There is a certain act of faith in assuming that the multipion background from hydrogen has the same shape versus χ^2 as the background from the dummy target under the two-body hydrogen signal. We believe that this is reasonable, since the shape of the background is governed largely by errors of measurement. However, it highlights the reason for being
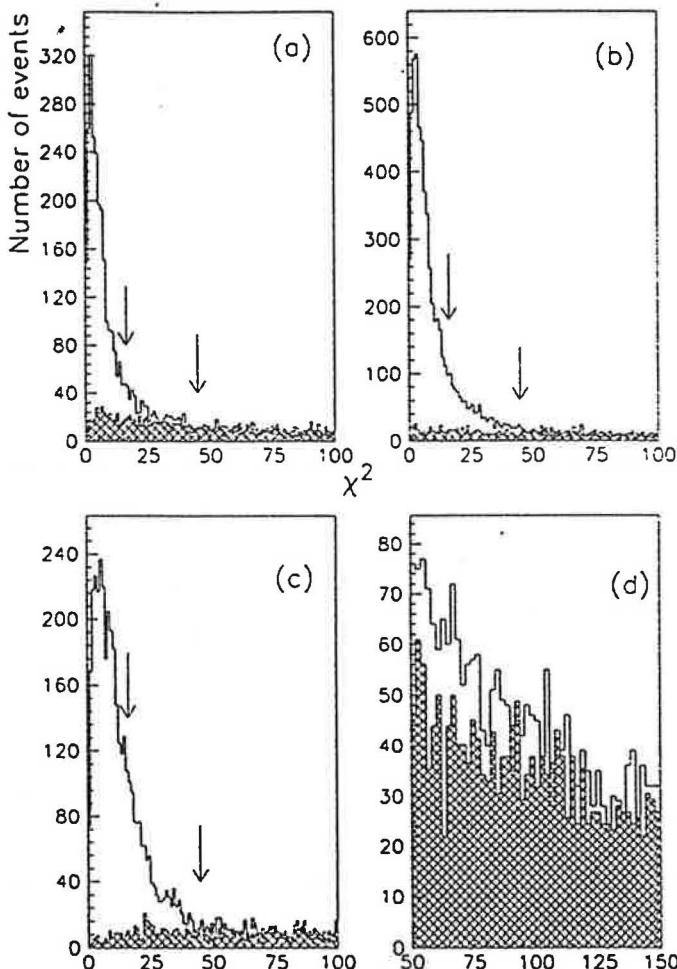
Fig. 5. Comparison of χ^2 distributions for signal and background at 1089 MeV/c for $\bar{p}p \rightarrow \pi^-\pi^+$: (a) 0°–20° and 160°–180° centre of mass. (b) 20°–60° and 120°–160°. (c) 60°–120°, (d) 0°–180°. Arrows indicate cuts for determining A_{0N} and dσ/dΩ. The full histogram shows data from the polarised target and the shaded histogram that from the dummy target.

fastidious over optimising the signal/background ratio. Errors in quoted results cover both statistical and estimated systematic errors in the background subtraction.

Further cuts are applied to restrict events to the target and eliminate as far as possible events from S3 and the cryostat walls. The vertex is determined from the weighted mean of the intersections of the three tracks: beam and exit particles. The beam track is generally reconstructed from coordinates upstream of the target in C- and J-chambers. However, because of the high rates in this region, some events contained double tracks. In these cases, the mean beam direction is
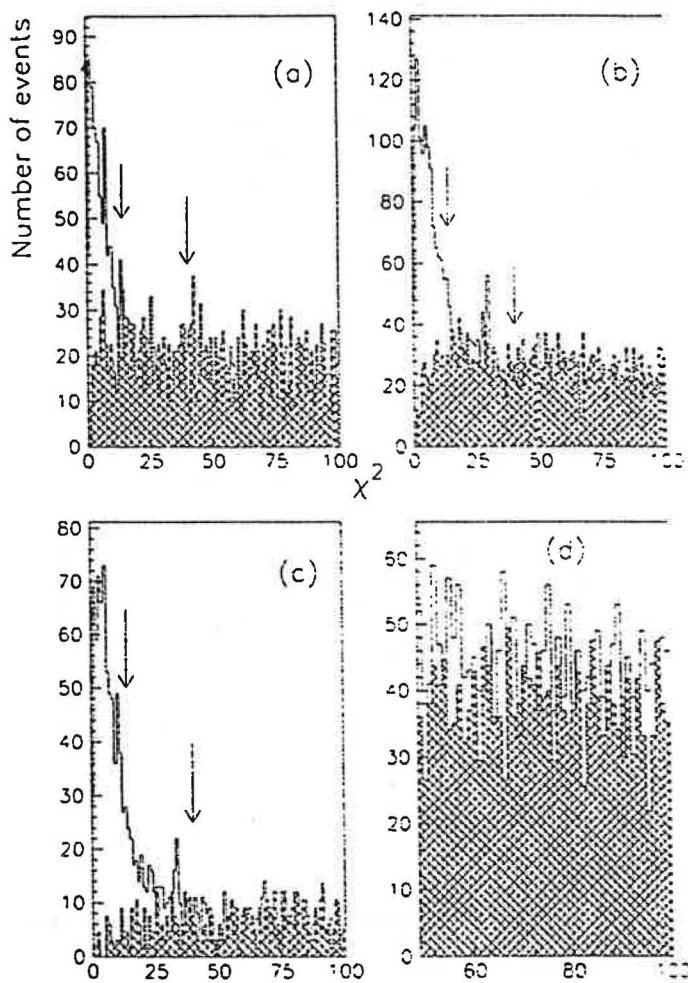
Fig. 6. As fig. 5 for $\bar{p}p \to \bar{K}K$.

assumed and a suitable error applied. Fig. 8 shows the vertex distribution reconstructed from all events: the dashed histogram shows the vertex calculated from events satisfying the $\pi\pi$ or $\bar{K}K$ kinematics. The target is clearly separated over most of the angular range, but events from S3 and the cryostat walls contribute to a small degree at extreme forward and backward angles. The increase in the number of events down the length of the target is a consequence of the increasing azimuthal acceptance, which is limited by the pole pieces of the magnet.

The number of events surviving to this final stage of analysis is typically 7500 $\pi\pi$ and 2100 $\bar{K}K$ per momentum from 493 to 1291 MeV/c and rather less at the lowest momenta (because of beam blow-up before S3) and at the highest momenta (because of the narrowly spaced momenta).
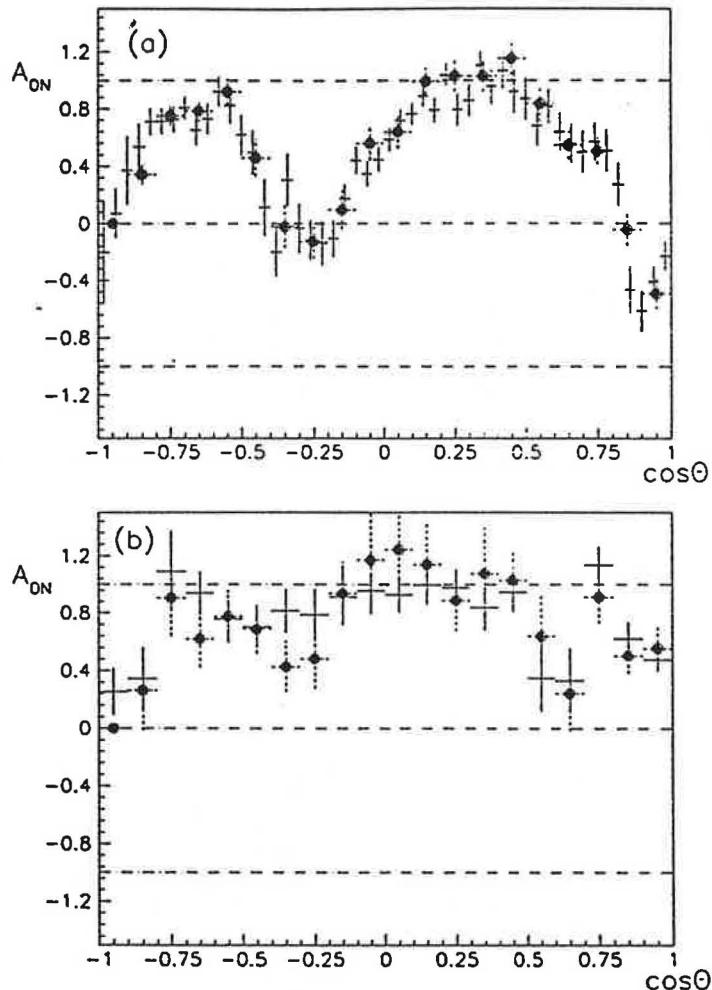
Fig. 7. Comparison of asymmetry results at 1351 MeV/c obtained (a) for $\bar{p}p \to \pi^-\pi^+$, (b) for $\bar{p}p \to K^-K^+$ from two independent analyses. Full circles are results without the correction for systematic biases in the geometry and crosses those with it.

3.5. EVALUATION OF RESULTS

In evaluating both dσ/dΩ and A_{0N}, straightforward allowance is made for differences in target polarisations, P, for spin up and spin down, starting from the equation

$$n = C(\mathrm{d}\sigma/\mathrm{d}\Omega)_0(1 + PA_{0N} \cos \phi).$$

where n is the number of events per incident $\bar{p}$ after background subtraction, ϕ is the azimuthal angle between the plane of the event and the horizontal, and C is a
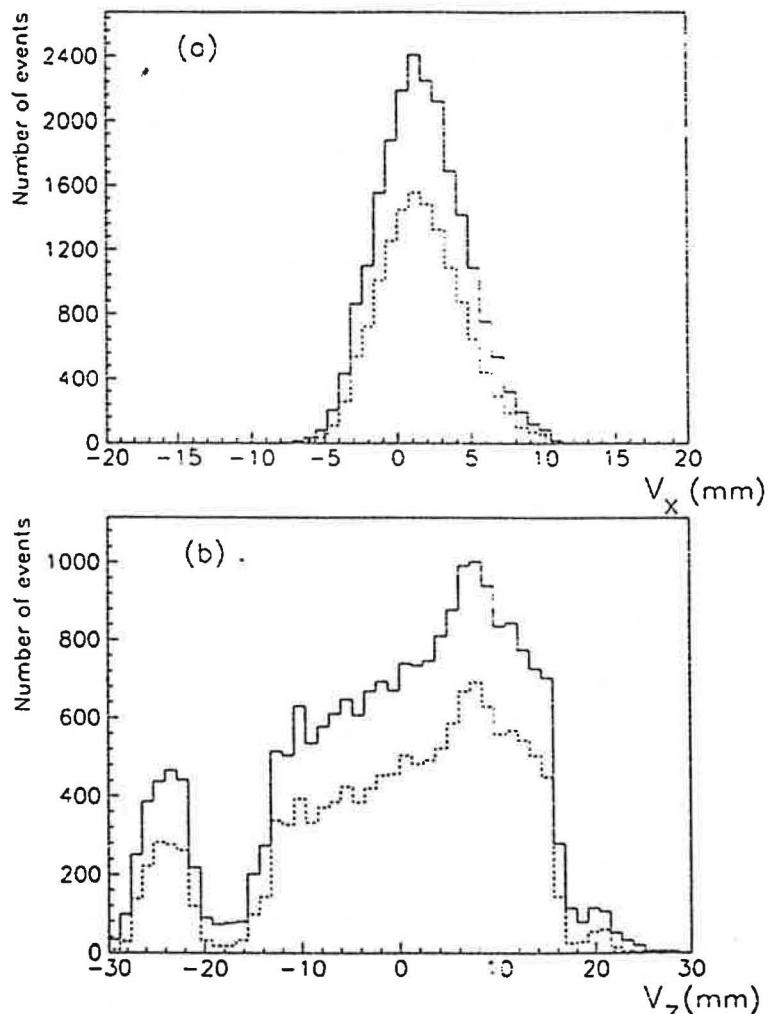
Fig. 8. Vertex distribution of events at 1089 MeV/c for $\theta_\pi = 20$ to 160°. The dashed line shows the distribution for events fitting $\pi\pi$ or $\bar{K}K$.

constant depending on solid angle and target mass; $(d\sigma/d\Omega)_0$ is the unpolarised cross section. Target polarisations are averaged through each run with a weight factor proportional to beam rate, which varied significantly over the spill.

Asymmetry results are evaluated from all events triggering S2 or S3, with a tiny correction for the mean value of cos ϕ; this correction is generally 1% but rises to 5% at extreme forward and backward angles, where the acceptance in ϕ is large. Differential cross sections are evaluated from events triggering S3. A strict cut is applied on ϕ to eliminate any possible losses of events outside the active areas of the chambers or events attenuated in pole-face vetos; a three-standard-deviation

margin is allowed for multiple scattering and measurement errors. The cut on ϕ varies with θ. Results are checked for stability against this cut.

Around $\theta = 90°$, two independent determinations of A_{0N} and $d\sigma/d\Omega$ are available from events to the left and right. These determinations agree within statistics.

In evaluating differential cross section, corrections made for beam attenuation to the target centre, i.e. in S2, S3, the cryostat and target material. The correction is up to 12.7% at low momenta. It is assumed that reaction cross sections on nuclei are shadowed by a factor $A^{1/3}$ compared with hydrogen, i.e. they scale as $A^{2/3}$. No
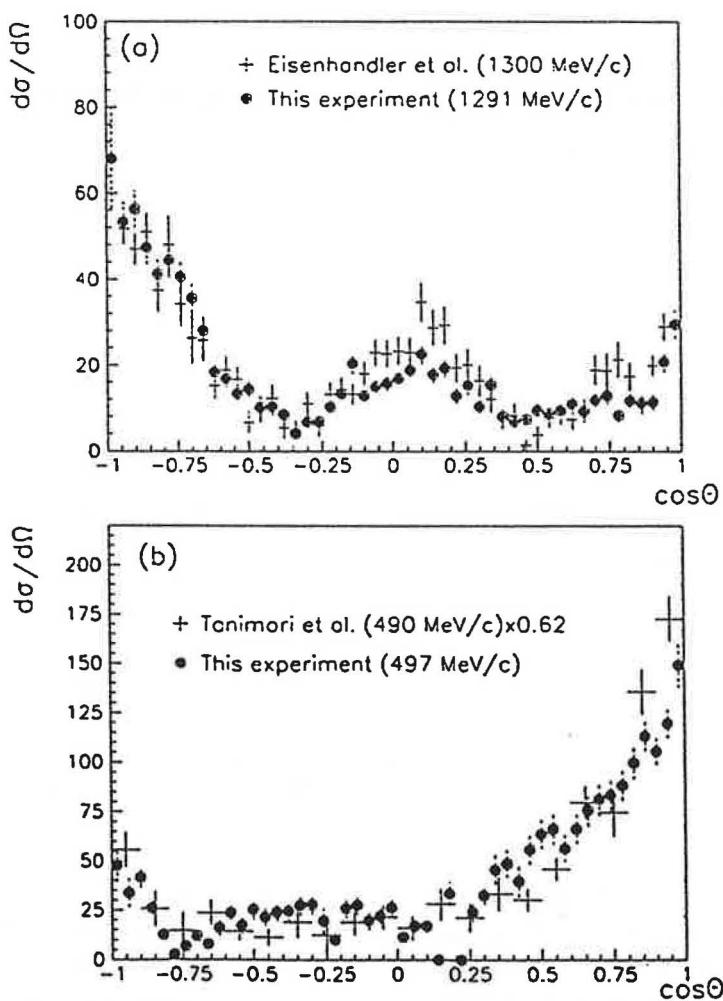
Fig. 9. Comparison of $d\sigma/d\Omega$ data (μb/sr) for $\bar{p}pi \to \pi^-\pi^+$ from this experiment with neighbouring momenta of Eisenhandler et al. [3] and Tanimori [11].

allowance is made for nuclear elastic scattering, which is through such small angles that beam is not lost.'

Corrections are also applied for decays and interactions of outgoing pions and kaons. These corrections vary little with scattering angle and beam momentum. Decay corrections are larger for backward particles than forward, but after allowing for losses of both, the overall corrections varies remarkably little with scattering angle. For pions it is within the range 1.76–0.88% and for kaons within the range 22.1–26.0%. The corrections for interactions are typically 3% for both $\pi^-\pi^+$ and K^-K^+.
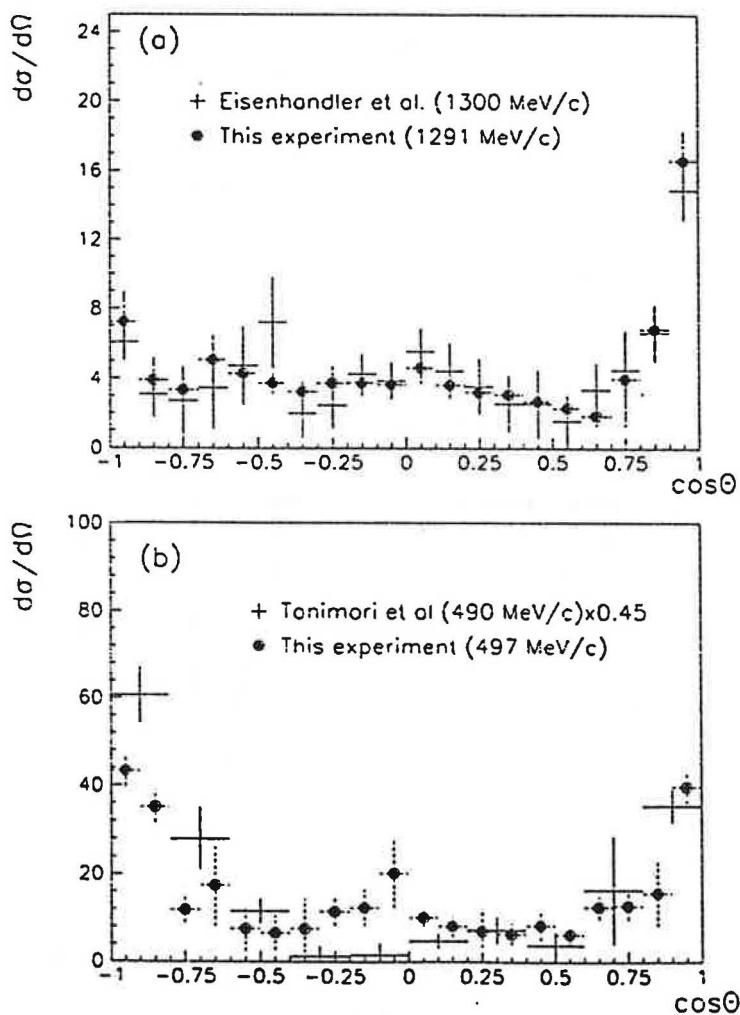
Fig. 10. Comparison of $d\sigma/d\Omega$ data (μb/sr) for p̄p → K⁻K⁺ from this experiment with neighbouring momenta of Eisenhandler et al. [3] and Tanimori [11].

4. Results

Results for $\bar{p}p \to \pi\pi$ agree well in shape with the earlier data of Eisenhandler et al., Tanimori et al. and Carter et al. The data of Tanimori et al. [12] are scaled by the factors given in their second paper [11]. Comparisons are given in figs. 9–11.

Later we shall show fits to the data with Legendre series. The first term a_0 in the fit to differential cross sections is a measure of the integrated cross section. Fig. 12 compares these integrated cross sections. There are clear normalisation discrepancies between our data, those of Eisenhandler et al. (higher for $\pi\pi$) and those of Tanimori et al. (slightly lower). However, we repeat the remark of sect. 2 that the normalisation uncertainty of our differential cross sections is about $\pm 10\%$ from uncertainties in the packing density of the polarised target. Despite the small statistical errors, one cannot conclude that there is any narrow structure in $\sigma(\bar{p}p \to \pi^-\pi^+)$. There could be a small effect in $\sigma(\bar{p}p \to K^-K^+)$ at 1420 MeV/c and we discuss this below. In both figs. 12a and b, our points scatter about a smooth curve by amounts rather above statistics. We have no precise explanation for this observation, but conjecture that it could arise from either (i) systematic
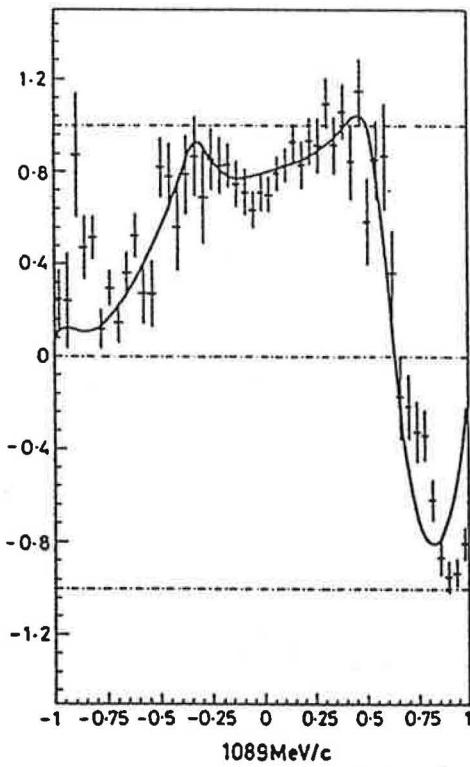
Fig. 11. Comparison of A_{0N} data from this experiment at 988 MeV/c with a fitted curve through those of Carter et al. [4].
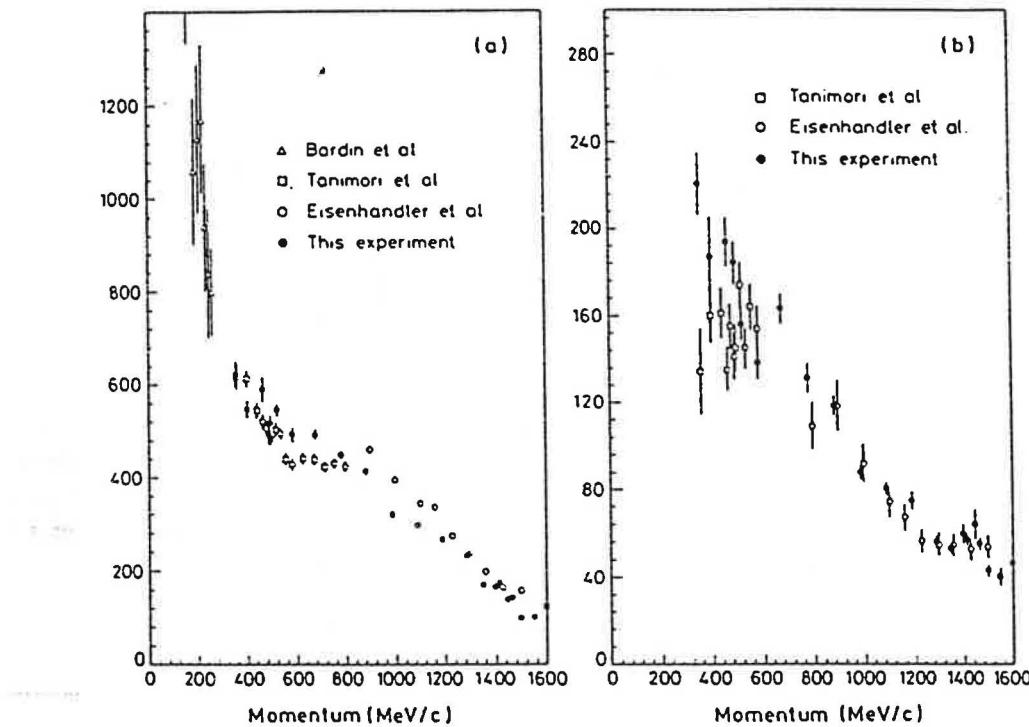
Fig. 12. Comparison of integrated cross sections (μb) with earlier data (a) $\bar{p}p \to \pi^-\pi^-$. (b) $\bar{p}p \to K^-K^-$.

errors in estimation of background under the $\pi\pi$ and $\overline{K}K$ signals, or (ii) variations between different momenta in the packing density of target material the beam traverses.

When one superimposes figs. 12a and b, it is clear that there is some significant variation with momentum of the $K^-K^+/\pi^-\pi^+$ cross-section ratio, $r_{K\pi}$. Fig. 13 shows this ratio from our data. There are slight peaks at the ends of the momentum range and a broad minimum around 950 MeV/c. Non-strange resonances with J up to 4 are known to cluster around a mass of 2050 MeV/c^2 (i.e. a momentum of 950 MeV/c) and corresponding $\bar{s}s$ resonances around 2200 MeV/c^2 ($\equiv$ 1350 MeV/c), so a variation of the ratio $r_{K\pi}$ such as fig. 13 describes would be compatible with coupling to these resonances.

Our results are displayed in figs. 14–21 and tables 3–6. The curves are fits with Legendre polynomials:

$$\frac{d\sigma}{d\Omega} = \sum a_i P_i(\cos\theta),$$

$$A_{0N}\frac{d\sigma}{d\Omega} = \sum b_i P_i^1(\cos\theta).$$
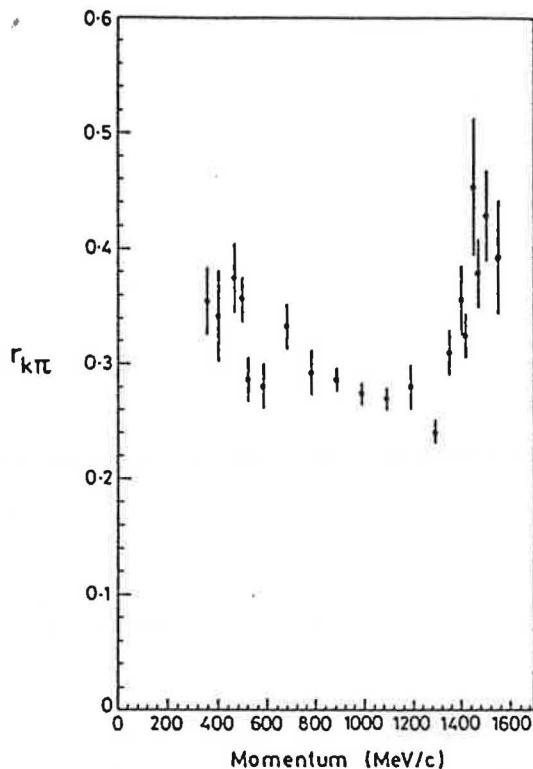
Fig. 13. The ratio of $r_{K\pi} = \sigma(\bar{p}p \to K^-K^+)/\sigma(\bar{p}p \to \pi^-\pi^+)$ from our data.

The latter form guarantees that $P \to 0$ at $0°$ and $180°$. Figs. 22–25 display Legendre coefficients, normalised to a_0, against momentum. In the $\overline{K}K$ case, minor penalty functions are necessary in the fit in order to ensure A_{0N} does not exceed 1.

There are several remarkable features in these results. Firstly, b_3 to b_6 for $\overline{K}K$ rise rapidly above 1200 MeV/c and so do a_8 and the magnitude of b_7 for $\pi\pi$. This is not unexpected in view of the $s\bar{s}$ resonances around 2200 MeV/c^2 (1350 MeV/c). However, we do not observe any narrow structure in $\overline{K}K$ results, associated with $\xi(2230)$.

Polarisations are remarkably high for both $\pi\pi$ and $\overline{K}K$. A polarisation close to unity can arise only from F_{++} and F_{+-} of similar magnitudes and $90°$ phase difference. Several inferences can be drawn for this. Firstly, it requires that some amplitudes have large imaginary parts. From analyticity, it is then very likely that amplitudes rotate round the Argand diagram with energy in a clockwise fashion, i.e. it is likely that resonances are present. Secondly, because the very large polarisations persist over a wide mass range, it is likely that resonances exhibit some coherence, such as the towers of resonances in the Veneziano model. Martin

$$d\sigma/d\Omega \ (\mu b/sr) \ for \ \bar{p}p \to \pi^-\pi^+$$
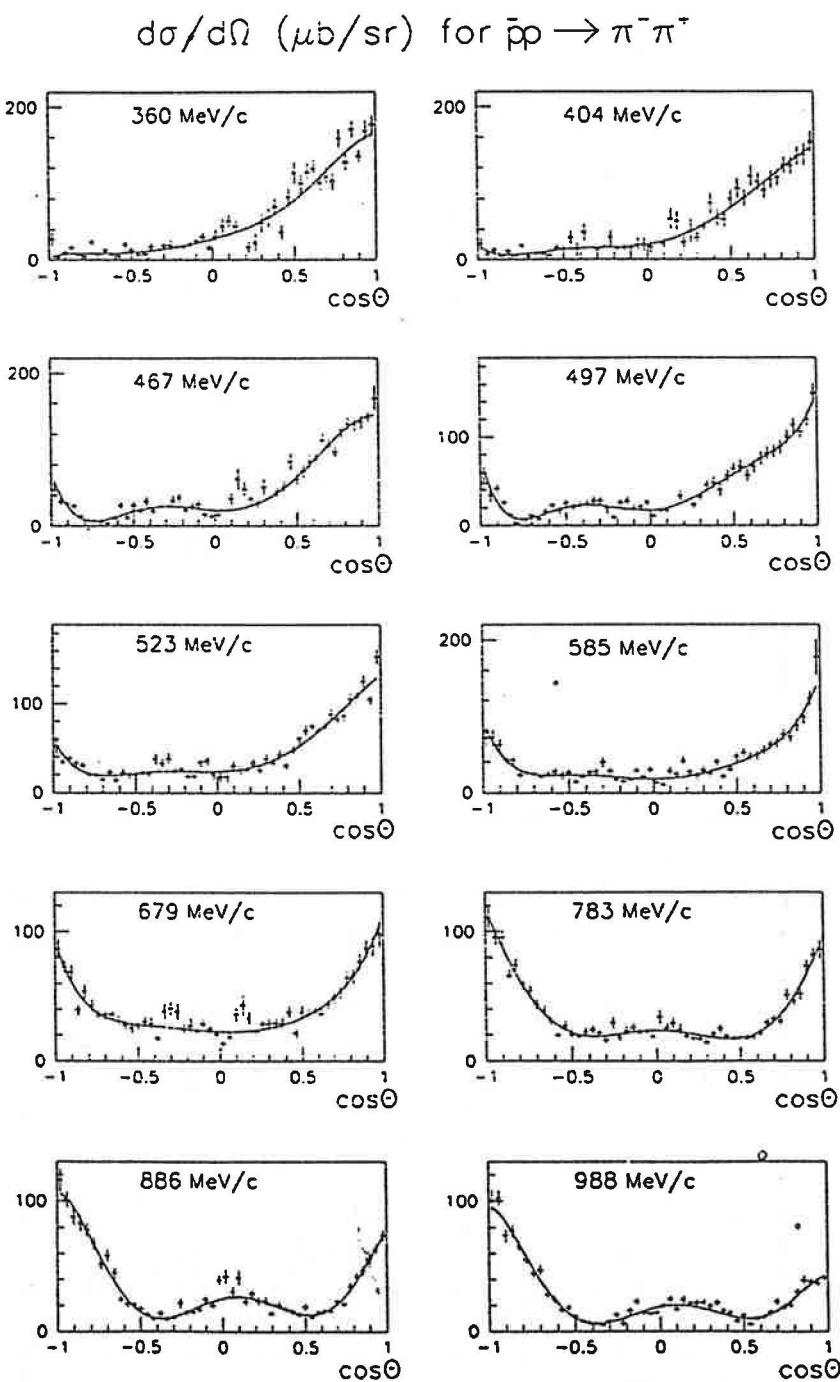
Fig. 14. $d\sigma/d\Omega(\bar{p}p \to \pi^-\pi^+)(\mu b/sr)$ from 360 to 988 MeV/c from this experiment. Smooth curves are fits with Legendre series.
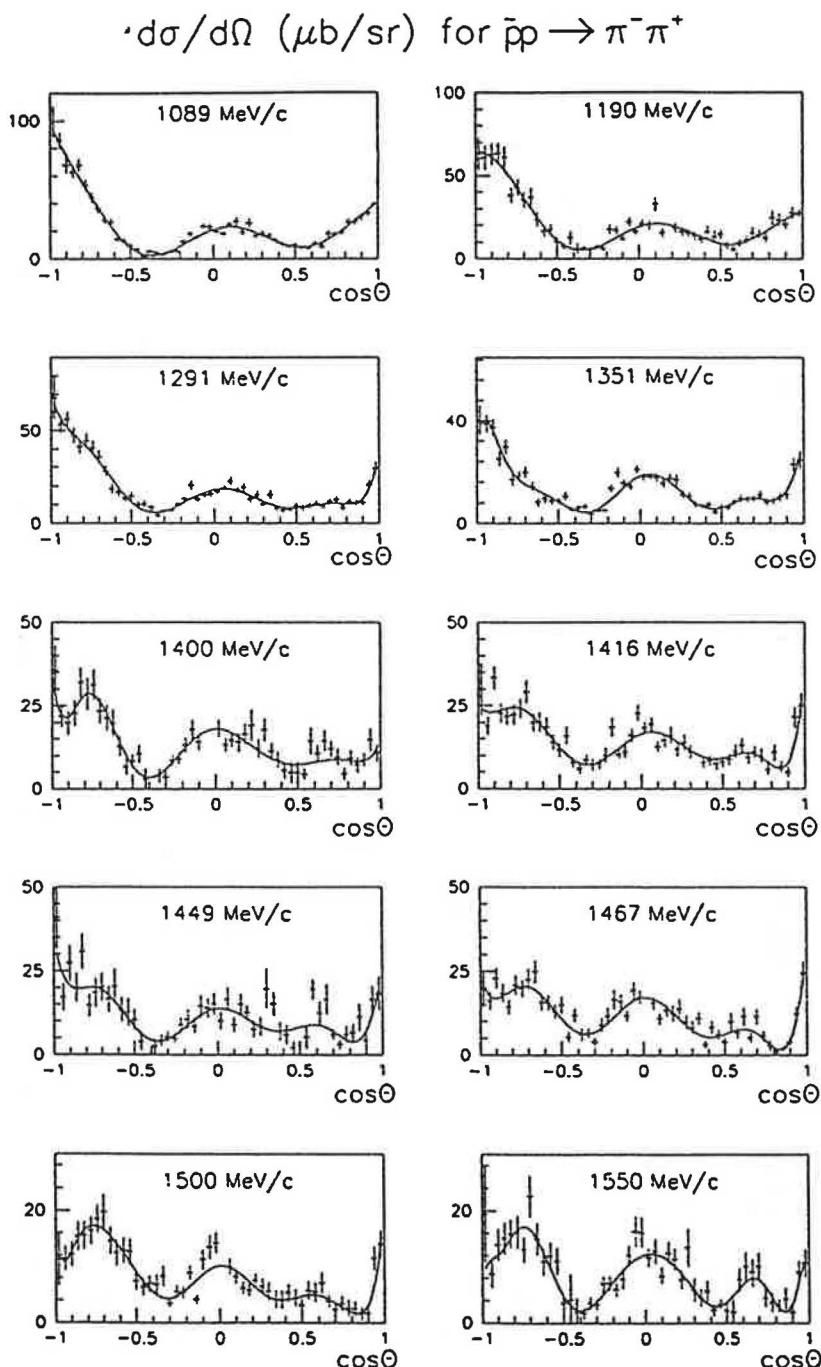
·dσ/dΩ (μb/sr) for p̄p → π⁻π⁺

Fig. 15. dσ/dΩ(p̄p → π⁻ π⁺)(μb/sr) from 1089 to 1550 MeV/c from this experiment. Smooth curves are fits with Legendre series.

A_{0N} for $\bar{p}p \to \pi^-\pi^+$
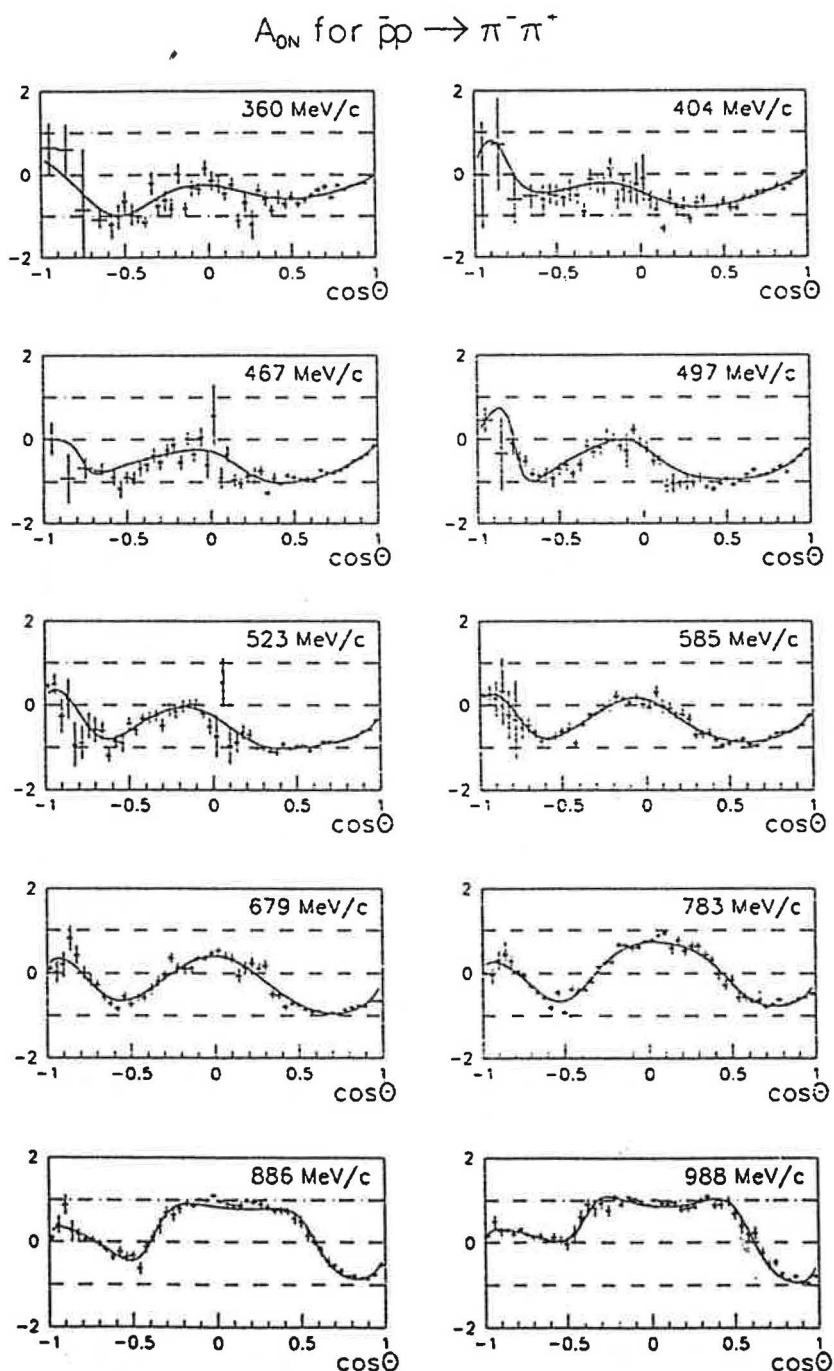
Fig. 16. $A_{0N}(\bar{p}p \to \pi^-\pi^+)$ from 360 to 988 MeV/c from this experiment. Smooth curves are fits to A_{0N} dσ dΩ with Legendre series.

A_{ON} for $\bar{p}p \to \pi^-\pi^+$

Fig. 17. $A_{ON}(\bar{p}p \to \pi^-\pi^+)$ from 1089 to 1550 MeV/c from this experiment. Smooth curves are fits to $A_{ON}\, d\sigma\, d\Omega$ with Legendre series.

$d\sigma/d\Omega$ $(\mu b/sr)$ for $\bar{p}p \to K^-K^+$
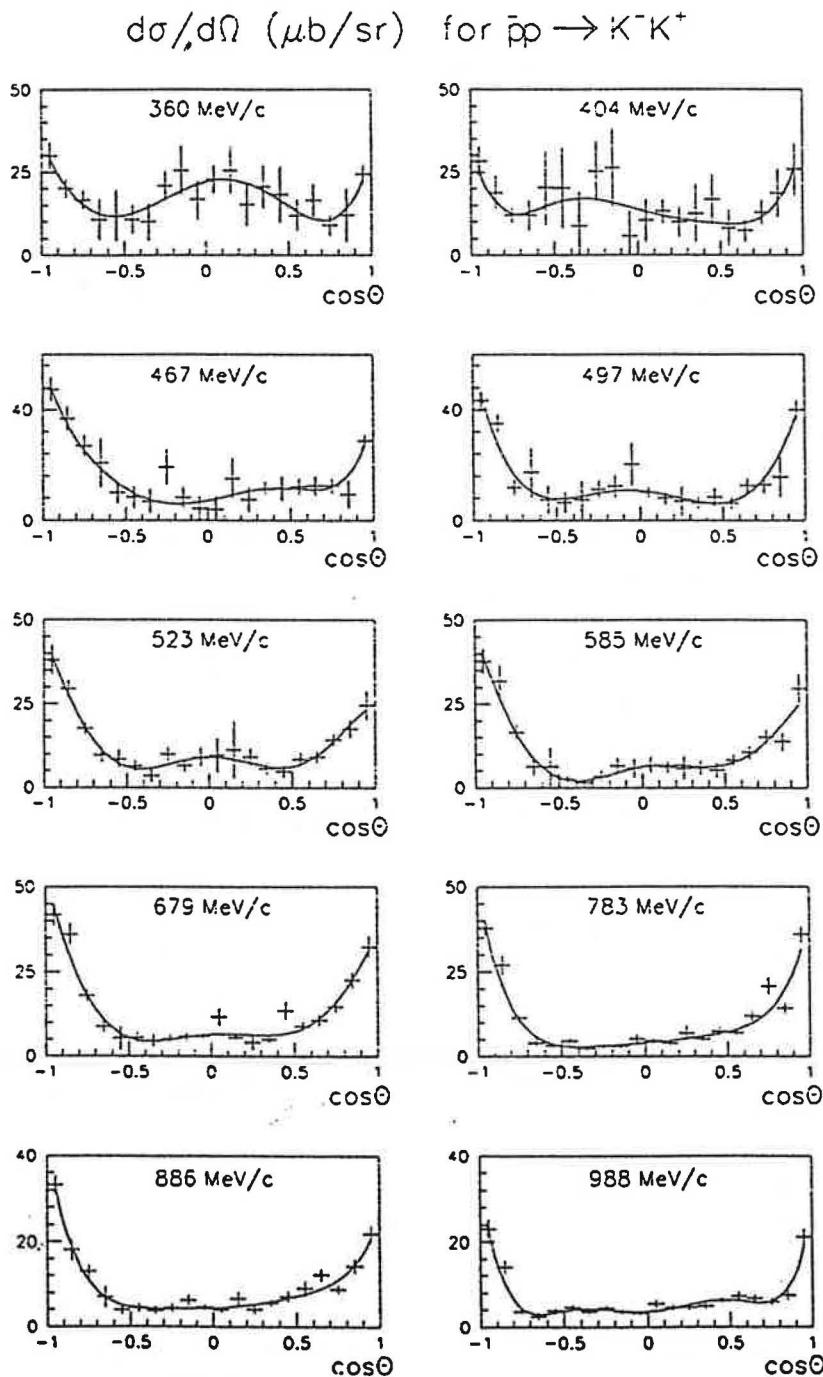
Fig. 18. $d\sigma/d\Omega(\bar{p}p \to K^-K^+ \, \mu b/sr)$ from 360 to 988 MeV/c from this experiment. Smooth curves are fits with Legendre series.

$d\sigma/d\Omega$ $(\mu b/sr)$ for $\bar{p}p \to K^-K^+$
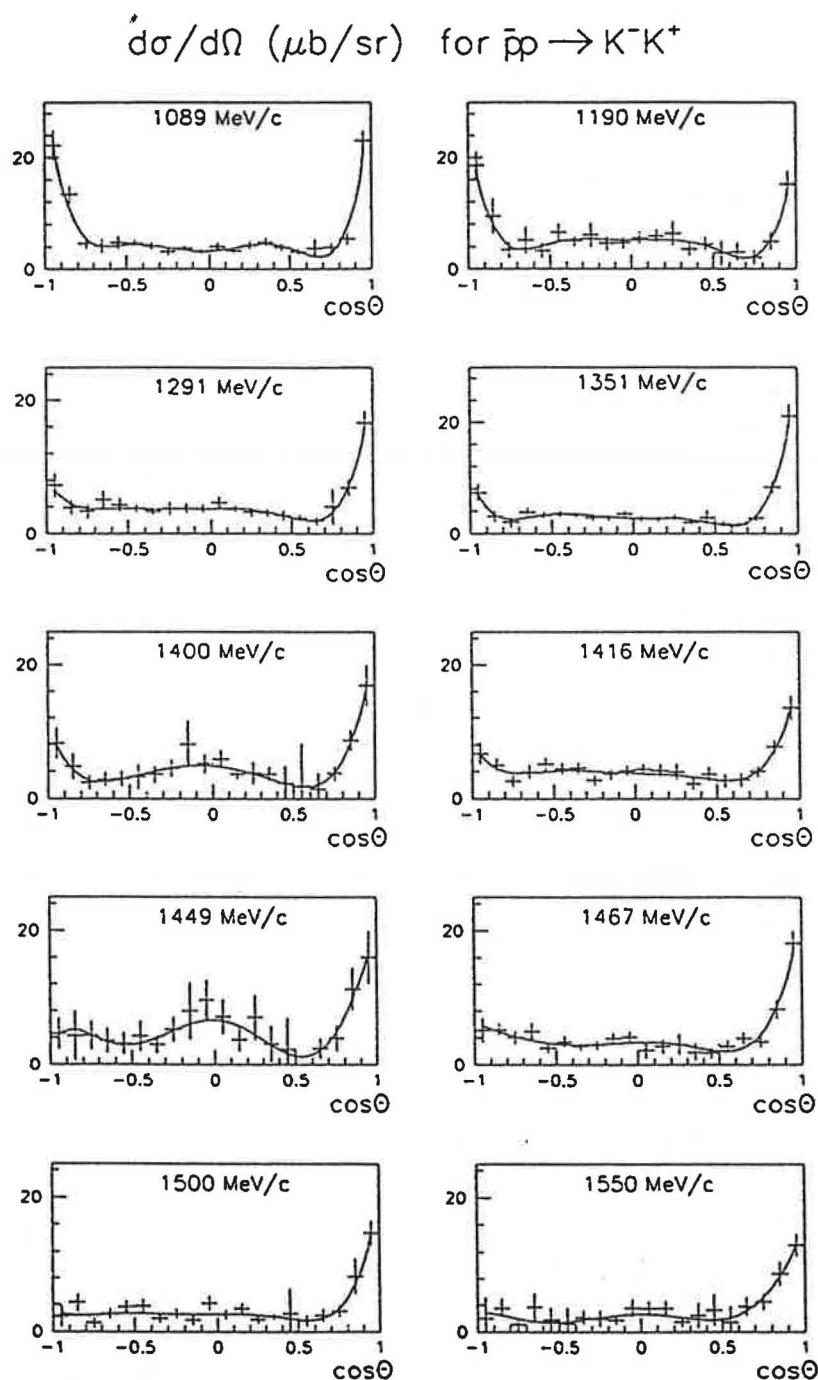
Fig. 19. $d\sigma/d\Omega(\bar{p}p \to K^-K^+)(\mu b/sr)$ from 1089 to 1550 MeV/c from this experiment. Smooth curves are fits with Legendre series.

A_{0N} for $\bar{p}p \to K^-K^+$
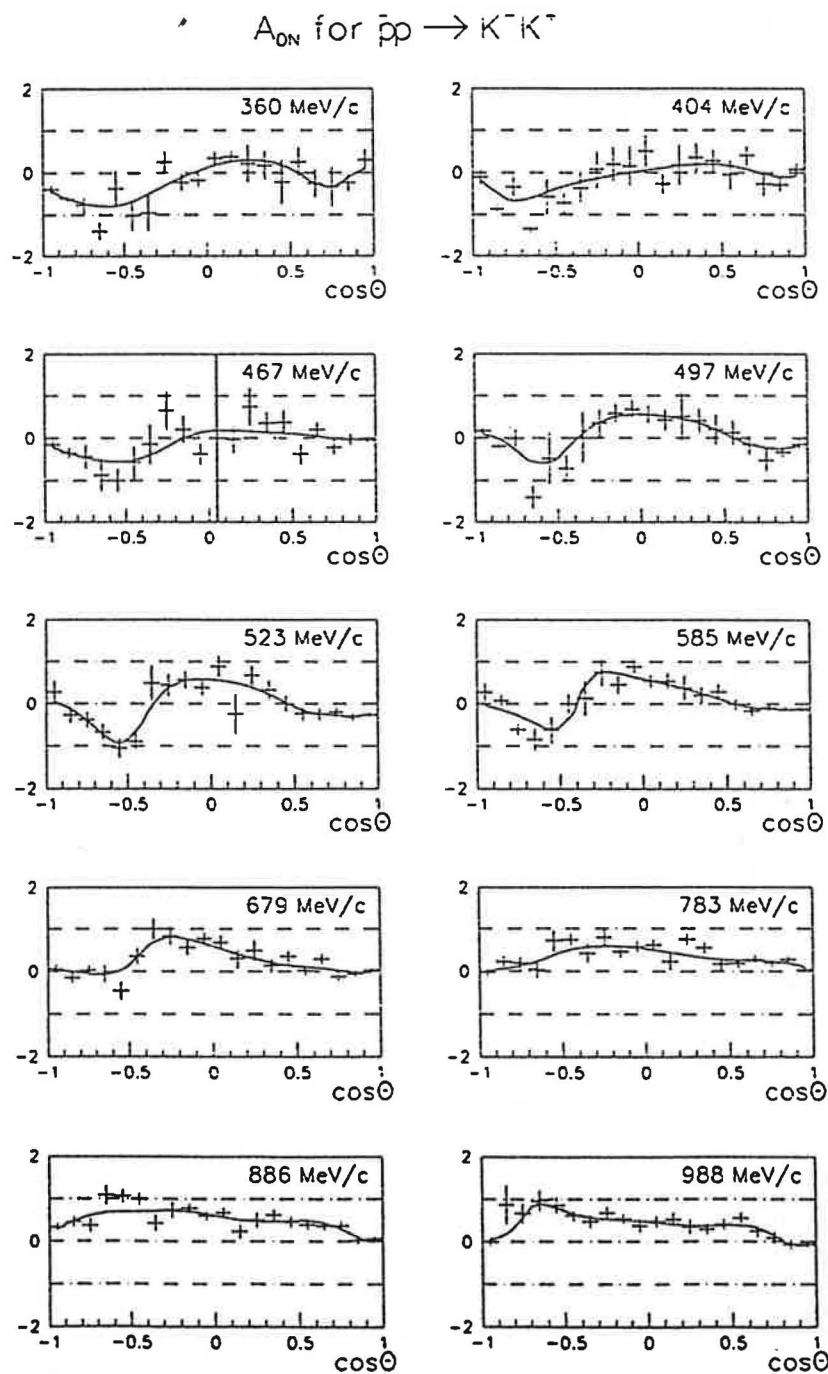
Fig. 20. $A_{0N}(\bar{p}p \to K^-K^+)$ from 360 to 988 MeV/c from this experiment. Smooth curves are fits to $A_{0N}\,d\sigma\,d\Omega$ with Legendre series.

A_ON for p̄p → K⁻K⁺
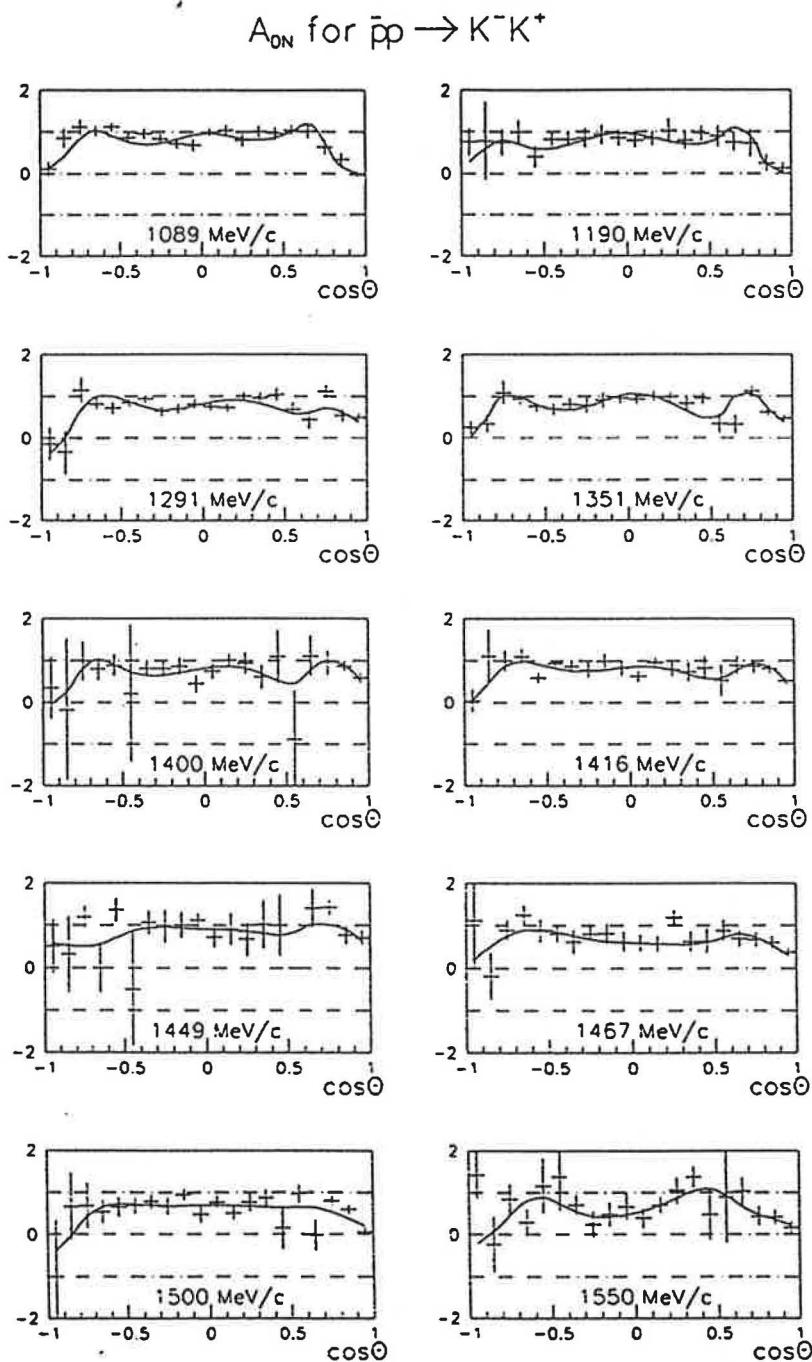
Fig. 21. A_ON(p̄p → K⁻K⁺) from 1089 to 1550 MeV/c from this experiment. Smooth curves are fits to A_ON dσ dΩ with Legendre series.

TABLE 3
Differential cross sections for $\bar{p}p \to \pi^-\pi^-$

cos θ^*	360 MeV/c		404 MeV/c		467 MeV/c		497 MeV/c		523 MeV/c	
	dσ/dΩ [μb/sr]	$\pm$	dσ/dΩ [μb/sr]	$\pm$	dσ/dΩ [μb/sr]	$\pm$	dσ/dΩ [μb/sr]	$\pm$	dσ/dΩ [μb/sr]	$\pm$
−0.97	27.17	9.78	20.57	8.80	46.90	9.52	47.78	8.78	52.04	8.61
−0.94	3.58	2.15	7.53	5.06	31.46	5.64	33.72	7.73	33.99	4.40
−0.90	10.19	3.23	13.42	4.09	29.22	5.05	41.63	5.56	38.66	4.24
−0.86	16.31	3.98	4.92	2.09	26.25	4.54	25.99	3.89	33.10	4.21
−0.82	7.06	2.67	11.42	4.69	13.43	3.32	12.56	2.63	30.68	3.94
−0.78	4.68	4.24	5.63	2.75	7.57	2.82	2.88	1.93	19.45	3.34
−0.74	23.58	5.30	18.60	3.15	7.18	2.25	6.93	2.14	19.95	3.38
−0.70	7.71	2.66	4.48	2.75	5.56	2.18	11.84	2.76	14.14	3.01
−0.66	13.17	4.48	8.77	4.21	3.76	2.31	7.87	2.47	23.00	4.19
−0.62	7.43	4.18	7.85	3.66	10.75	3.62	16.01	4.38	13.63	3.28
−0.58	4.70	3.01	5.82	3.48	26.80	6.21	23.54	4.10	22.13	4.51
−0.54	20.56	5.30	15.60	5.57	11.41	4.62	17.31	4.98	19.74	4.78
−0.50	13.46	4.50	13.95	6.66	26.77	6.08	25.20	5.37	19.38	4.13
−0.46	7.41	3.74	29.31	9.54	19.93	4.90	21.45	5.05	21.53	4.14
−0.42	7.76	3.23	13.79	9.24	32.16	6.76	23.94	4.90	21.07	4.46
−0.38	17.36	5.99	36.01	12.19	19.36	5.00	24.51	5.72	37.77	6.59
−0.34	0.00	0.00	0.00	0.00	0.00	0.00	27.53	5.46	24.72	5.43
−0.30	19.48	5.88	14.19	4.29	0.00	0.00	27.82	5.38	34.67	7.16
−0.26	19.34	8.28	16.52	5.45	22.64	7.90	19.54	6.49	24.45	4.88
−0.22	17.14	5.65	29.42	11.10	26.88	6.91	9.97	3.22	26.45	5.27
−0.18	17.14	5.65	15.34	4.74	20.36	4.47	26.07	5.22	18.18	3.66
−0.14	19.98	4.95	15.30	4.78	26.04	5.91	27.62	5.18	18.08	3.39
−0.10	25.38	6.00	15.12	4.50	28.40	5.43	19.79	5.03	34.21	5.69
−0.06	30.30	6.39	20.22	9.46	14.79	5.14	22.03	4.42	35.45	5.52
−0.02	16.08	4.88	20.22	9.46	12.90	4.37	26.28	4.52	19.90	5.66
0.02	31.03	9.07	16.39	8.30	14.56	4.79	11.44	2.86	17.56	6.28
0.06	44.19	11.37	0.00	0.00	0.00	0.00	16.97	3.42	17.56	6.28
0.10	50.82	9.34	21.17	7.31	35.60	8.32	16.96	3.35	29.95	6.70
0.14	44.38	8.93	33.43	14.75	30.89	15.14	0.00	0.00	25.27	6.48
0.18	0.00	0.00	40.66	12.72	27.79	9.70	33.51	6.13	25.58	4.55
0.22	26.85	7.97	22.84	8.05	35.23	8.64	0.00	0.00	33.56	5.39
0.26	42.96	11.49	37.38	17.31	29.70	6.97	24.04	5.25	25.29	5.26
0.30	48.23	13.16	28.62	7.65	50.77	11.06	32.52	4.94	38.38	5.78
0.34	55.32	12.81	43.38	9.74	0.00	0.00	45.65	7.62	33.23	4.87
0.38	69.35	11.95	73.91	14.86	44.37	7.33	48.72	7.14	42.99	5.39
0.42	56.83	10.32	54.40	11.91	51.34	8.34	39.79	8.30	30.58	4.85
0.46	82.03	12.13	52.59	10.51	84.29	11.53	55.91	7.66	47.16	5.73
0.50	113.34	14.88	78.92	12.68	60.75	8.81	63.75	7.72	61.22	6.75
0.54	99.87	13.00	92.99	13.63	71.70	9.17	66.36	8.32	69.39	6.66
0.58	114.02	13.85	80.49	11.68	84.45	10.52	56.44	7.35	74.73	6.91
0.62	118.63	13.55	109.49	13.82	86.56	9.60	66.37	7.76	69.33	6.60
0.66	100.34	11.74	101.90	12.78	112.18	11.00	75.98	8.40	73.79	6.71
0.70	108.57	12.89	90.54	11.33	105.04	10.64	81.55	8.63	88.48	7.16
0.74	102.33	11.79	104.64	12.21	96.67	9.60	83.72	8.10	82.44	6.11
0.78	157.90	13.35	107.50	11.54	125.16	10.81	88.47	7.76	86.30	6.75
0.82	127.49	11.43	123.08	11.31	133.02	11.24	99.84	8.41	105.51	7.85
0.86	170.96	11.50	122.40	12.69	132.34	9.42	113.27	8.04	107.99	6.72
0.90	134.90	8.42	134.97	12.91	135.52	9.50	105.51	6.82	125.95	7.10
0.94	168.53	13.66	136.83	14.98	142.79	7.49	119.77	7.71	104.77	6.09
0.97	176.51	13.20	153.43	14.84	167.06	17.33	149.21	11.74	153.53	8.62

TABLE 3 (continued)

cos θ^*	585 MeV/c		679 MeV/c		783 MeV/c		886 MeV/c		988 MeV/c	
	$d\sigma/d\Omega$ [μb/sr]	$\pm$	$d\sigma/d\Omega$ [μb/sr]	$\pm$	$d\sigma/d\Omega$ [μb/sr]	$\pm$	$d\sigma/d\Omega$ [μb/sr]	$\pm$	$d\sigma/d\Omega$ [μb/sr]	$\pm$
−0.97	71.25	9.81	86.69	8.06	110.89	9.47	115.60	8.88	100.60	8.83
−0.94	71.92	10.58	72.70	5.40	95.45	6.21	101.11	6.60	102.44	6.19
−0.90	61.64	7.91	69.15	5.74	95.38	6.19	88.33	6.65	73.90	5.08
−0.86	42.51	6.81	39.60	4.56	65.59	5.41	82.85	6.38	77.33	5.13
−0.82	42.27	6.53	53.78	5.57	74.28	5.15	78.29	5.78	65.81	4.37
−0.78	22.52	4.50	43.24	5.03	59.73	4.60	67.86	4.99	55.50	3.86
−0.74	25.11	3.92	34.90	4.20	53.69	4.56	51.81	4.40	44.71	3.45
−0.70	24.43	4.00	35.97	4.47	43.51	4.17	58.68	4.88	47.10	3.74
−0.66	20.35	4.01	36.18	4.70	38.90	4.18	45.03	4.22	27.99	2.85
−0.62	23.14	4.92	30.81	4.06	30.92	3.73	24.63	3.25	24.54	2.86
−0.58	27.48	5.31	27.70	4.03	19.79	2.97	20.90	2.99	16.33	2.39
−0.54	22.39	5.72	25.24	4.01	27.51	3.57	20.75	3.00	18.02	2.47
−0.50	26.51	4.84	27.65	4.02	20.05	3.07	17.23	2.92	11.76	2.13
−0.46	14.21	3.43	30.45	4.24	18.94	2.82	13.01	2.45	8.21	1.72
−0.42	20.31	4.30	29.03	4.94	22.44	3.58	9.39	2.04	6.59	1.44
−0.38	26.85	4.95	17.89	3.28	23.81	3.56	13.97	2.77	6.16	1.53
−0.34	27.50	4.76	34.10	6.35	21.63	3.50	9.28	2.05	4.57	1.23
−0.30	39.68	7.23	22.61	5.91	16.03	2.65	10.27	2.18	7.86	1.68
−0.26	28.10	6.54	34.19	6.97	29.24	4.99	21.61	4.41	12.61	2.66
−0.22	16.72	3.85	24.37	4.45	18.09	3.51	14.20	2.74	6.12	2.31
−0.18	14.56	3.08	27.46	5.57	23.36	3.77	14.44	1.98	16.05	2.81
−0.14	16.71	3.26	23.00	3.28	26.06	3.29	16.49	2.00	18.86	2.73
−0.10	28.69	3.89	28.65	3.69	22.45	2.78	25.03	3.02	14.26	1.74
−0.06	20.84	3.15	24.84	3.23	23.09	2.81	20.01	2.43	13.58	1.66
−0.02	30.07	4.31	20.90	3.04	19.07	2.25	32.52	4.36	14.16	1.54
0.02	13.04	2.76	13.55	2.53	34.38	5.54	0.00	0.00	19.87	1.99
0.06	10.82	2.40	18.41	3.44	25.78	4.22	30.15	4.83	24.68	2.72
0.10	28.10	6.07	26.03	6.04	29.43	4.63	33.35	6.53	16.72	1.90
0.14	24.70	5.36	37.01	8.40	24.43	4.32	22.64	3.19	24.11	3.27
0.18	41.25	7.06	33.21	5.56	19.47	3.58	29.22	4.02	21.35	2.59
0.22	27.32	6.30	22.97	3.75	18.00	3.47	23.26	3.76	21.65	2.89
0.26	22.10	5.01	28.54	4.53	17.16	3.27	23.35	3.76	21.80	3.06
0.30	29.40	6.79	28.58	4.60	14.40	2.95	13.68	2.52	19.36	2.99
0.34	24.84	5.56	29.20	4.68	21.19	3.46	20.39	3.24	21.63	2.84
0.38	40.19	6.22	29.06	4.76	24.97	4.01	17.49	2.97	16.04	2.30
0.42	20.79	4.25	37.80	5.02	19.32	3.13	15.52	2.69	14.01	2.34
0.46	30.01	5.02	21.32	3.67	17.83	2.99	12.93	2.65	7.81	1.73
0.50	46.53	6.52	37.51	5.36	18.15	2.62	19.09	3.15	12.36	2.10
0.54	51.68	6.76	35.93	5.23	17.55	2.68	10.95	2.20	5.44	1.32
0.58	45.95	6.70	37.73	5.05	18.11	2.71	14.76	2.39	9.86	1.91
0.62	48.37	6.43	36.30	4.85	21.37	2.84	15.55	2.83	11.06	1.95
0.66	54.46	6.82	43.74	5.05	29.45	3.21	15.63	2.77	15.05	2.44
0.70	62.55	6.75	49.10	5.67	32.44	3.28	22.93	2.87	22.74	2.72
0.74	64.88	7.09	52.83	5.46	30.78	3.26	21.01	2.93	18.56	2.35
0.78	75.53	7.67	64.06	6.08	51.05	4.73	34.91	4.03	19.83	2.54
0.82	72.85	7.71	66.02	6.44	46.51	3.87	42.71	4.13	30.18	2.84
0.86	87.40	8.36	77.17	6.42	51.62	4.05	47.09	4.27	39.27	3.37
0.90	97.86	9.29	87.41	6.84	72.92	4.95	55.95	4.57	38.03	3.19
0.94	122.30	10.21	88.60	7.22	81.79	5.01	63.69	4.05	36.73	2.62
0.97	176.72	23.67	97.95	10.62	85.84	7.30	73.88	4.42	41.33	2.46

TABLE 3 (continued)

cos θ^*	1089 MeV/c		1190 MeV/c		1291 MeV/c		1351 MeV/c		1400 MeV/c	
	dσ/dΩ [μb/sr]	$\pm$	dσ/dΩ [μb/sr]	$\pm$	dσ/dΩ [μb/sr]	$\pm$	dσ/dΩ [μb/sr]	$\pm$	dσ/dΩ [μb/sr]	$\pm$
−0.97	99.41	11.40	63.08	10.00	68.01	11.84	40.29	5.99	35.74	7.35
−0.94	85.58	5.74	60.80	7.28	53.29	4.70	38.84	3.65	21.90	3.46
−0.90	67.76	5.45	62.79	6.78	56.24	4.43	37.56	3.26	19.90	3.65
−0.86	62.58	4.16	63.64	6.21	47.37	4.17	25.09	2.88	22.80	4.01
−0.82	67.79	4.48	61.12	6.69	41.15	3.69	29.72	3.02	32.07	4.41
−0.78	53.31	3.99	38.19	4.67	44.45	4.30	16.85	2.52	28.61	4.92
−0.74	44.32	3.87	42.90	5.18	40.58	3.83	18.37	2.17	31.31	4.72
−0.70	36.33	3.36	35.40	4.83	35.57	3.60	19.85	2.26	23.37	3.98
−0.66	27.66	2.97	37.12	5.32	28.03	3.27	14.33	2.11	21.36	3.97
−0.62	26.41	3.07	23.65	4.64	18.37	2.79	8.32	1.86	19.84	4.15
−0.58	14.10	2.20	16.55	3.69	16.81	2.48	9.63	1.91	12.76	3.10
−0.54	13.00	2.11	17.54	3.49	13.36	2.24	8.67	1.56	6.61	2.52
−0.50	9.53	1.82	10.56	2.83	14.40	2.26	8.87	1.53	8.28	2.15
−0.46	6.60	1.46	7.42	2.28	10.12	2.09	10.54	1.70	10.50	2.76
−0.42	2.03	0.76	12.50	4.10	10.29	2.26	5.49	1.27	3.00	3.16
−0.38	5.76	1.59	5.93	3.38	8.49	1.94	6.22	1.37	0.00	0.00
−0.34	4.81	1.27	6.34	2.24	4.07	0.99	6.60	1.26	3.99	2.07
−0.30	3.47	0.96	5.50	1.38	6.69	1.09	3.80	0.76	3.48	2.00
−0.26	5.15	0.96	6.92	1.86	6.81	1.19	4.79	0.86	8.61	1.74
−0.22	5.80	0.98	5.89	1.56	10.28	1.54	5.03	0.81	9.04	1.73
−0.18	12.84	1.60	17.95	3.32	13.25	1.63	13.56	1.63	13.16	2.51
−0.14	18.14	2.49	17.12	2.85	20.38	2.70	19.82	2.13	17.84	2.99
−0.10	15.41	1.86	11.90	2.09	12.84	1.60	15.63	1.65	14.00	2.37
−0.06	23.45	2.45	22.11	3.17	14.96	1.71	14.25	1.45	0.00	0.00
−0.02	23.23	2.36	16.23	2.28	15.76	1.97	21.02	1.78	0.00	0.00
0.02	19.83	1.89	20.95	2.92	16.88	1.71	17.90	1.62	18.16	2.79
0.06	18.12	1.76	20.24	3.06	18.81	1.95	17.95	1.61	13.18	2.14
0.10	25.04	2.19	0.00	0.00	22.56	2.45	17.68	1.78	14.63	2.22
0.14	27.13	3.32	15.57	2.99	17.83	2.18	15.40	1.70	14.02	2.97
0.18	19.22	2.39	0.00	0.00	19.30	2.20	17.45	2.10	16.57	3.27
0.22	25.88	3.29	18.51	3.41	12.80	2.20	16.97	2.27	19.12	4.87
0.26	16.58	2.25	16.32	3.06	15.29	2.48	11.04	1.79	12.12	3.06
0.30	18.52	2.59	15.39	3.01	10.32	1.84	10.53	1.67	17.75	3.63
0.34	16.69	2.24	13.95	3.13	15.36	2.69	7.29	1.45	11.24	2.85
0.38	13.53	2.04	11.93	2.72	8.02	1.92	6.92	1.31	8.70	2.56
0.42	10.88	1.95	16.18	3.86	6.85	1.65	7.39	1.57	5.49	2.66
0.46	8.85	1.71	13.17	4.23	7.32	1.58	4.29	1.13	4.91	3.40
0.50	10.12	1.74	14.73	3.08	9.46	1.84	6.44	1.36	4.91	3.40
0.54	8.18	1.69	8.18	2.77	8.61	2.07	6.27	1.32	4.39	1.68
0.58	7.70	1.62	5.95	1.90	9.47	1.95	8.48	1.52	14.37	4.18
0.62	11.27	1.91	9.87	2.59	10.92	1.92	9.71	1.63	10.57	2.59
0.66	8.77	1.72	11.53	2.72	9.19	1.80	9.58	1.50	14.50	3.34
0.70	18.02	2.43	15.80	3.31	11.85	1.98	9.67	1.47	11.93	2.67
0.74	17.70	2.28	14.66	3.20	12.83	2.08	11.00	1.80	9.56	2.62
0.78	19.18	2.38	12.57	2.77	8.29	1.81	8.43	1.69	4.44	2.04
0.82	26.82	2.75	24.72	4.48	11.63	1.98	8.91	1.70	9.30	2.49
0.86	26.56	2.83	23.41	4.07	11.11	1.94	10.25	1.87	7.11	2.51
0.90	30.33	3.15	20.90	3.38	11.31	2.03	11.16	1.92	8.69	2.25
0.94	33.05	2.75	27.60	3.86	20.80	2.53	22.93	2.70	14.74	3.55
0.97	39.65	1.32	27.44	2.48	29.57	3.45	24.70	3.45	10.69	2.86

A. Hasan et al. / $\bar{p}p \to \pi^+\pi^-, K^-K^+$

TABLE 3 (continued)

cos θ*	1416 MeV/c		1449 MeV/c		1467 MeV/c		1500 MeV/c		1550 MeV/c	
	dσ/dΩ [μb/sr]	±	dσ/dΩ [μb/sr]	±	dσ/dΩ [μb/sr]	±	dσ/dΩ [μb/sr]	±	dσ/dΩ [μb/sr]	±
−0.97	29.95	7.99	40.89	9.34	19.80	5.72	11.27	4.78	19.32	8.66
−0.94	18.88	2.88	17.14	4.27	16.18	2.85	11.45	2.29	8.67	2.54
−0.90	33.35	3.62	27.45	5.45	22.93	3.25	12.17	2.25	13.98	2.95
−0.86	22.65	2.97	20.09	4.47	18.42	3.03	15.38	2.69	15.08	2.97
−0.82	21.67	2.82	30.73	5.52	14.34	2.35	15.52	2.52	15.89	2.59
−0.78	22.31	3.27	14.70	3.61	20.91	3.07	16.42	2.62	16.19	3.06
−0.74	24.14	3.00	18.45	4.50	19.95	2.74	18.49	2.58	13.05	2.41
−0.70	29.08	3.74	20.12	4.40	22.65	3.35	19.72	3.21	22.58	3.75
−0.66	19.93	2.91	16.54	4.10	24.94	3.56	14.57	2.55	14.93	3.00
−0.62	20.03	3.08	20.37	5.36	15.83	2.68	12.46	2.43	10.89	2.56
−0.58	18.57	2.95	13.37	3.82	15.63	2.48	12.80	2.28	11.95	2.49
−0.54	13.96	2.40	12.57	4.37	13.06	2.39	12.67	2.39	11.02	2.50
−0.50	11.56	2.28	10.40	3.32	15.00	2.70	7.39	1.69	3.64	1.29
−0.46	15.88	2.79	3.93	2.87	5.42	1.70	6.29	1.57	4.17	4.60
−0.42	7.78	1.70	0.00	0.00	11.86	2.26	6.97	1.60	1.98	2.42
−0.38	5.93	1.66	2.52	2.73	6.14	1.98	6.80	1.91	1.76	1.16
−0.34	8.51	1.85	4.30	1.93	6.50	1.58	8.30	1.96	3.57	1.17
−0.30	7.16	1.82	5.27	1.87	3.99	1.39	3.44	0.85	3.26	0.99
−0.26	7.41	1.72	4.88	1.52	9.04	2.30	5.58	1.29	6.94	1.53
−0.22	10.09	2.29	8.92	2.38	11.69	2.75	5.33	1.25	7.07	1.44
−0.18	0.00	0.00	10.51	3.04	16.61	3.11	8.84	1.35	5.97	1.37
−0.14	10.25	1.53	8.56	2.33	16.10	2.27	4.19	0.92	7.78	1.84
−0.10	10.91	1.86	14.49	3.46	11.61	1.85	11.27	1.89	12.11	1.92
−0.06	16.09	2.27	13.96	3.12	19.28	2.82	13.47	2.22	16.37	2.81
−0.02	22.70	2.58	15.23	3.42	17.33	2.10	14.17	2.03	16.12	2.91
0.02	18.25	2.01	10.17	2.69	0.00	0.00	0.00	0.00	11.69	1.77
0.06	19.37	2.21	16.64	3.56	15.53	2.05	9.94	1.66	12.80	2.28
0.10	12.60	1.73	8.93	2.48	10.83	1.80	8.21	1.34	8.41	1.63
0.14	14.47	2.11	15.13	3.26	13.28	1.93	6.17	1.23	12.44	2.18
0.18	15.98	2.66	12.62	2.35	12.49	2.80	5.78	1.11	11.33	2.06
0.22	11.82	2.30	7.59	2.57	13.86	2.95	7.47	1.35	7.73	1.72
0.26	13.83	2.49	8.47	2.86	9.87	2.37	6.51	1.40	13.43	3.54
0.30	11.06	2.17	19.80	6.27	8.12	2.13	5.61	1.88	5.94	2.16
0.34	0.00	0.00	15.25	3.73	10.89	1.96	4.18	1.62	4.56	1.70
0.38	7.90	1.83	7.08	3.00	3.23	1.42	4.13	1.74	5.70	1.93
0.42	8.44	1.83	5.92	3.11	8.22	2.13	5.30	1.59	2.38	1.17
0.46	7.47	1.92	2.03	2.14	6.00	1.75	4.34	1.68	3.39	0.98
0.50	7.99	1.72	0.00	0.00	4.04	1.28	3.14	1.12	2.27	1.48
0.54	8.83	1.90	5.21	3.51	9.98	2.75	5.75	1.76	1.95	2.31
0.58	11.22	2.10	19.60	3.20	6.57	1.79	5.47	1.86	7.84	2.18
0.62	13.05	2.27	12.51	3.48	11.55	2.73	7.06	2.05	10.11	2.64
0.66	9.51	2.04	16.66	4.74	5.13	1.58	3.85	1.27	9.08	2.59
0.70	10.98	1.94	5.98	1.80	11.47	2.34	2.40	1.28	10.19	2.44
0.74	9.82	2.29	3.14	1.60	5.60	1.79	3.47	1.49	4.54	1.72
0.78	5.75	1.83	6.10	2.85	2.85	1.76	2.64	1.52	3.72	1.72
0.82	10.91	2.49	6.57	2.79	1.05	1.28	2.53	1.31	3.13	1.25
0.86	6.66	1.76	11.20	4.38	2.13	1.03	1.64	1.18	4.35	1.99
0.90	4.82	1.66	4.20	2.26	4.03	1.37	1.78	1.07	1.93	1.38
0.94	21.55	3.22	16.65	4.05	12.26	2.21	11.53	2.16	9.03	2.15
0.97	25.00	3.72	18.27	5.26	24.37	3.84	14.06	2.56	10.69	2.58

TABLE 4

Aymmetries for $\bar{p}p \rightarrow \pi^+\pi^-$

$\cos \theta^*$	360 MeV/c		404 MeV/c		467 MeV/c		497 MeV/c		523 MeV/c	
	A_{0N}	±	A_{0N}	±	A_{0N}	±	A_{0N}	±	A_{0N}	±
−0.97	0.95	0.90	0.16	2.06	−0.06	0.44	0.73	0.37	0.45	0.10
−0.94	0.11	0.71	−1.19	4.82	1.45	1.37	−1.01	1.23	0.49	0.25
−0.90	−0.04	1.07	0.63	1.02	−1.50	3.41	0.03	0.89	−0.26	0.41
−0.86	1.55	1.89	1.32	2.30	−0.37	1.38	−0.96	1.29	0.14	0.49
−0.82	0.76	0.72	0.09	1.17	−1.04	0.57	0.73	1.06	−0.93	0.54
−0.78	−1.40	1.51	−1.34	3.09	−0.83	0.34	−0.09	0.33	−0.89	0.42
−0.74	−0.04	1.96	0.09	0.94	−0.75	0.40	−0.45	0.18	−0.49	0.31
−0.70	−1.40	1.73	−0.37	0.76	−0.42	0.58	−0.52	0.17	−0.58	0.31
−0.66	−1.19	0.34	−1.01	0.31	−0.84	0.27	−0.82	0.15	−0.61	0.23
−0.62	−0.98	0.33	−0.11	0.51	−0.64	0.24	−0.86	0.15	−1.19	0.15
−0.58	−1.21	0.35	−0.60	0.36	−0.91	0.20	−0.81	0.17	−0.86	0.16
−0.54	−1.03	0.33	−0.48	0.26	−1.16	0.22	−0.93	0.22	−0.89	0.24
−0.50	−0.65	0.27	−0.51	0.28	−0.91	0.17	−0.70	0.17	−0.43	0.16
−0.46	−0.95	0.29	−0.56	0.26	−0.94	0.17	−0.60	0.17	−0.60	0.15
−0.42	−1.02	0.17	−0.38	0.28	−0.69	0.19	−0.81	0.15	−0.32	0.15
−0.38	−1.15	0.16	−0.51	0.24	−0.60	0.21	−0.60	0.18	−0.30	0.15
−0.34	−0.21	0.29	−0.90	0.21	−0.37	0.19	−0.16	0.16	−0.25	0.16
−0.30	−0.76	0.22	−0.12	0.27	−0.54	0.21	−0.30	0.22	−0.48	0.18
−0.26	−0.61	0.27	−0.23	0.26	−0.26	0.20	−0.19	0.23	−0.11	0.18
−0.22	−0.82	0.24	−0.23	0.28	−0.12	0.20	0.00	0.26	−0.15	0.17
−0.18	0.02	0.26	0.14	0.26	−0.55	0.20	0.01	0.15	−0.03	0.16
−0.14	−0.81	0.16	−0.62	0.26	0.02	0.17	−0.16	0.15	0.01	0.13
−0.10	−0.31	0.22	−0.37	0.34	−0.35	0.19	−0.27	0.43	0.02	0.14
−0.06	−0.34	0.17	−0.43	0.29	0.06	0.24	0.23	0.15	−0.20	0.14
−0.02	0.15	0.20	−0.25	0.53	−0.61	0.33	−0.09	0.16	−0.50	0.21
0.02	−0.14	0.24	−0.10	0.58	0.57	0.73	−0.20	0.17	−0.74	0.52
0.06	−0.25	0.21	−0.63	0.24	−0.91	0.26	−0.51	0.13	0.54	0.59
0.10	−0.46	0.16	−0.86	0.22	−0.35	0.21	−0.48	0.17	−0.96	0.46
0.14	−0.23	0.17	−1.31	0.12	−0.96	0.16	−1.11	0.18	−0.89	0.23
0.18	−1.11	0.22	−0.60	0.23	−1.03	0.13	−1.05	0.24	−0.64	0.18
0.22	−0.68	0.24	−0.81	0.17	−0.89	0.14	−1.02	0.16	−0.69	0.13
0.26	−1.21	0.37	−0.82	0.29	−0.86	0.23	−1.00	0.20	−1.03	0.11
0.30	−0.38	0.17	−1.07	0.14	−0.74	0.15	−1.00	0.14	−1.02	0.10
0.34	−0.59	0.19	−0.70	0.19	−1.26	0.09	−0.91	0.13	−1.09	0.08
0.38	−0.87	0.14	−0.58	0.16	−0.93	0.14	−1.13	0.09	−1.12	0.09
0.42	−0.55	0.19	−1.00	0.11	−1.06	0.09	−1.18	0.10	−0.92	0.10
0.46	−0.71	0.13	−0.77	0.12	−0.86	0.09	−1.06	0.09	−1.03	0.08
0.50	−0.52	0.13	−0.65	0.13	−0.91	0.11	−0.93	0.10	−0.97	0.08
0.54	−0.70	0.13	−0.80	0.12	−0.94	0.09	−1.07	0.09	−0.94	0.07
0.58	−0.61	0.11	−0.81	0.10	−0.92	0.10	−0.99	0.08	−1.08	0.07
0.62	−0.48	0.11	−0.57	0.11	−0.95	0.08	−0.83	0.08	−0.99	0.07
0.66	−0.37	0.10	−0.55	0.10	−0.72	0.08	−0.71	0.08	−0.87	0.07
0.70	−0.29	0.09	−0.43	0.09	−0.79	0.08	−0.86	0.09	−0.86	0.07
0.74	−0.55	0.08	−0.40	0.09	−0.80	0.07	−0.81	0.08	−0.88	0.06
0.78	−0.26	0.07	−0.37	0.09	−0.74	0.07	−0.72	0.08	−0.84	0.06
0.82	−0.37	0.07	−0.27	0.09	−0.65	0.07	−0.64	0.08	−0.79	0.06
0.86	−0.28	0.06	−0.37	0.08	−0.50	0.07	−0.77	0.07	−0.74	0.06
0.90	−0.24	0.05	−0.24	0.07	−0.44	0.06	−0.53	0.06	−0.62	0.05
0.94	−0.21	0.05	−0.11	0.07	−0.36	0.06	−0.40	0.05	−0.58	0.05
0.97	−0.03	0.06	0.05	0.09	−0.15	0.07	−0.24	0.06	−0.35	0.07

A. Hasan et al. / $\bar{p}p \to \pi^-\pi^-, K^-K^+$

TABLE 4 (continued)

$\cos\theta^*$	585 MeV/c		679 MeV/c		783 MeV/c		886 MeV/c		988 MeV/c	
	A_{0N}	±	A_{0N}	±	A_{0N}	±	A_{0N}	±	A_{0N}	±
−0.97	0.24	0.11	0.11	0.10	0.01	0.09	0.10	0.08	0.17	0.09
−0.94	0.24	0.22	0.04	0.26	−0.05	0.22	0.41	0.22	0.50	0.15
−0.90	0.16	0.44	0.20	0.31	0.31	0.24	0.88	0.25	0.28	0.14
−0.86	0.33	0.81	0.82	0.30	0.43	0.33	0.27	0.25	0.29	0.08
−0.82	−0.23	0.60	0.43	0.23	0.28	0.20	0.18	0.15	0.19	0.07
−0.78	−0.35	0.95	0.02	0.18	0.05	0.11	0.07	0.09	0.32	0.07
−0.74	−0.52	0.31	−0.17	0.15	−0.05	0.09	0.07	0.09	0.19	0.08
−0.70	−0.48	0.21	−0.28	0.12	−0.31	0.08	−0.03	0.09	0.13	0.08
−0.66	−0.63	0.20	−0.56	0.11	−0.46	0.09	−0.17	0.09	0.16	0.10
−0.62	−0.85	0.14	−0.71	0.10	−0.58	0.08	−0.36	0.10	0.06	0.10
−0.58	−0.80	0.12	−0.84	0.10	−0.82	0.08	−0.22	0.11	0.12	0.13
−0.54	−0.72	0.13	−0.55	0.12	−0.45	0.10	−0.35	0.12	0.04	0.14
−0.50	−0.61	0.12	−0.73	0.11	−0.93	0.08	−0.31	0.14	−0.04	0.17
−0.46	−0.54	0.17	−0.57	0.11	−0.38	0.12	−0.62	0.15	0.21	0.22
−0.42	−0.90	0.11	−0.58	0.13	−0.42	0.12	−0.11	0.16	0.61	0.19
−0.38	−0.46	0.13	−0.38	0.15	−0.39	0.12	0.14	0.15	0.91	0.16
−0.34	−0.21	0.15	−0.19	0.16	−0.21	0.13	0.38	0.21	0.81	0.19
−0.30	−0.20	0.15	−0.04	0.13	0.15	0.15	0.71	0.16	0.94	0.16
−0.26	−0.09	0.17	0.36	0.14	0.25	0.15	0.66	0.16	0.76	0.15
−0.22	−0.01	0.17	0.14	0.13	0.26	0.13	0.79	0.13	1.09	0.08
−0.18	0.21	0.15	0.09	0.12	0.67	0.10	0.91	0.09	0.90	0.10
−0.14	0.17	0.11	0.12	0.10	0.67	0.09	0.86	0.08	1.08	0.06
−0.10	0.07	0.11	0.35	0.10	0.59	0.09	1.01	0.07	1.04	0.08
−0.06	0.18	0.11	0.35	0.10	0.61	0.08	0.99	0.06	0.93	0.07
−0.02	0.03	0.11	0.47	0.10	0.76	0.08	1.10	0.05	0.90	0.07
0.02	−0.05	0.13	0.52	0.12	0.77	0.09	0.97	0.06	1.02	0.06
0.06	0.31	0.17	0.39	0.14	0.88	0.09	0.91	0.08	0.93	0.07
0.10	−0.04	0.18	0.34	0.14	0.94	0.09	0.88	0.10	0.92	0.08
0.14	−0.07	0.15	−0.07	0.18	0.59	0.15	0.87	0.10	0.95	0.08
0.18	−0.20	0.14	0.14	0.16	0.76	0.12	0.99	0.08	0.79	0.09
0.22	−0.22	0.16	0.23	0.15	0.52	0.12	0.95	0.08	0.81	0.10
0.26	−0.32	0.16	0.12	0.13	0.65	0.11	0.90	0.09	0.85	0.09
0.30	−0.69	0.13	0.17	0.15	0.63	0.12	0.84	0.10	1.01	0.10
0.34	−0.67	0.12	−0.50	0.12	0.43	0.12	0.75	0.10	1.09	0.08
0.38	−0.65	0.11	−0.53	0.12	0.30	0.12	0.75	0.11	0.88	0.11
0.42	−0.82	0.09	−0.79	0.09	−0.03	0.14	0.73	0.12	0.90	0.12
0.46	−0.94	0.07	−0.73	0.10	−0.28	0.14	0.56	0.14	0.98	0.13
0.50	−0.90	0.09	−0.76	0.09	−0.16	0.13	0.48	0.14	0.68	0.15
0.54	−0.84	0.08	−0.87	0.08	−0.57	0.12	0.16	0.16	0.40	0.21
0.58	−0.79	0.08	−0.91	0.07	−0.56	0.13	0.04	0.14	0.20	0.18
0.62	−0.92	0.07	−0.89	0.07	−0.66	0.11	−0.19	0.14	0.22	0.15
0.66	−0.96	0.06	−0.98	0.06	−0.63	0.09	−0.44	0.15	−0.25	0.14
0.70	−0.85	0.06	−0.94	0.06	−0.79	0.08	−0.55	0.10	−0.52	0.11
0.74	−0.75	0.07	−0.95	0.06	−0.72	0.08	−0.68	0.10	−0.46	0.11
0.78	−0.66	0.06	−0.86	0.06	−0.62	0.07	−0.79	0.07	−0.73	0.09
0.82	−0.63	0.06	−0.80	0.06	−0.75	0.07	−0.79	0.07	−0.88	0.07
0.86	−0.64	0.06	−0.75	0.05	−0.68	0.06	−0.85	0.06	−0.79	0.07
0.90	−0.55	0.06	−0.78	0.05	−0.60	0.06	−0.87	0.05	−0.93	0.06
0.94	−0.47	0.05	−0.65	0.06	−0.58	0.05	−0.77	0.05	−0.94	0.05
0.97	−0.23	0.07	−0.28	0.06	−0.47	0.06	−0.53	0.07	−0.78	0.07

TABLE 4 (continued)

cos θ*	1089 MeV/c		1190 MeV/c		1291 MeV/c		1351 MeV/c		1400 MeV/c	
	A_{0N}	±	A_{0N}	±	A_{0N}	±	A_{0N}	±	A_{0N}	±
−0.97	0.25	0.13	−0.55	0.30	0.02	0.13	−0.20	0.36	−0.09	0.32
−0.94	0.24	0.21	0.02	0.40	0.22	0.21	0.07	0.18	0.22	0.58
−0.90	0.87	0.28	0.62	0.51	0.35	0.14	0.37	0.24	0.57	0.80
−0.86	0.47	0.14	0.21	0.24	0.18	0.09	0.53	0.16	0.43	0.24
−0.82	0.52	0.09	0.21	0.13	0.47	0.08	0.71	0.10	0.83	0.13
−0.78	0.12	0.09	0.15	0.13	0.39	0.08	0.71	0.09	0.66	0.14
−0.74	0.30	0.08	0.56	0.12	0.48	0.08	0.73	0.09	0.63	0.14
−0.70	0.14	0.09	0.57	0.12	0.72	0.07	0.81	0.08	0.85	0.12
−0.66	0.36	0.10	0.65	0.12	0.57	0.09	0.65	0.11	1.08	0.12
−0.62	0.52	0.10	0.47	0.16	0.62	0.10	0.73	0.11	0.82	0.15
−0.58	0.27	0.14	0.47	0.16	0.58	0.10	0.92	0.11	0.71	0.17
−0.54	0.27	0.15	0.57	0.17	0.93	0.09	0.83	0.13	0.25	0.33
−0.50	0.82	0.13	0.49	0.21	0.63	0.13	0.62	0.14	0.48	0.22
−0.46	0.78	0.15	0.44	0.26	0.63	0.15	0.50	0.16	0.54	0.33
−0.42	0.56	0.20	1.18	0.16	0.12	0.18	0.11	0.20	0.00	0.00
−0.38	0.79	0.17	0.33	0.37	0.06	0.17	−0.20	0.18	0.00	0.00
−0.34	0.87	0.17	0.49	0.33	−0.10	0.16	0.31	0.19	0.05	0.33
−0.30	0.69	0.21	−0.30	0.33	0.04	0.16	−0.03	0.18	0.11	0.37
−0.26	0.85	0.14	−0.13	0.26	0.18	0.13	−0.12	0.15	0.23	0.21
−0.22	0.83	0.13	0.60	0.23	0.16	0.11	−0.14	0.16	−0.33	0.19
−0.18	0.83	0.10	0.38	0.19	0.41	0.10	−0.10	0.13	0.25	0.20
−0.14	0.75	0.10	0.42	0.17	0.32	0.10	0.18	0.10	0.11	0.17
−0.10	0.71	0.10	0.74	0.15	0.31	0.10	0.44	0.10	0.43	0.17
−0.06	0.63	0.09	0.49	0.14	0.40	0.10	0.35	0.09	0.08	0.15
−0.02	0.71	0.08	0.46	0.13	0.61	0.08	0.45	0.09	0.53	0.15
0.02	0.70	0.08	0.65	0.13	0.57	0.08	0.59	0.08	0.48	0.14
0.06	0.79	0.08	0.52	0.14	0.72	0.08	0.72	0.08	0.63	0.13
0.10	0.83	0.07	0.58	0.13	0.75	0.07	0.77	0.08	0.59	0.13
0.14	0.93	0.08	0.78	0.15	0.56	0.08	0.89	0.08	0.67	0.14
0.18	0.83	0.11	0.74	0.12	0.81	0.09	0.79	0.09	0.78	0.15
0.22	0.93	0.10	0.87	0.12	0.75	0.09	1.04	0.08	0.61	0.19
0.26	0.91	0.12	0.76	0.15	1.03	0.09	0.80	0.12	0.95	0.17
0.30	1.09	0.11	0.97	0.14	0.85	0.12	0.86	0.12	0.55	0.22
0.34	0.91	0.13	0.74	0.18	0.97	0.11	1.10	0.11	1.09	0.16
0.38	1.06	0.13	1.03	0.17	0.96	0.12	0.96	0.13	0.90	0.29
0.42	0.84	0.17	1.21	0.12	0.92	0.17	1.07	0.13	1.25	0.18
0.46	1.15	0.14	1.26	0.08	0.87	0.15	0.92	0.16	0.34	0.90
0.50	0.58	0.19	1.02	0.17	1.13	0.09	0.87	0.15	1.37	3.44
0.54	0.85	0.18	0.91	0.21	0.78	0.17	0.68	0.15	0.18	0.50
0.58	0.87	0.24	0.39	0.32	0.50	0.16	0.82	0.13	1.09	0.17
0.62	0.36	0.19	0.57	0.21	0.33	0.14	0.64	0.14	0.53	0.26
0.66	−0.17	0.18	0.06	0.25	0.56	0.17	0.56	0.14	0.39	0.33
0.70	−0.21	0.14	0.05	0.21	0.49	0.17	0.50	0.15	1.25	0.11
0.74	−0.33	0.13	0.22	0.20	0.33	0.14	0.57	0.14	0.45	0.29
0.78	−0.34	0.11	0.00	0.18	0.08	0.18	0.51	0.15	0.30	0.31
0.82	−0.62	0.09	−0.37	0.16	−0.33	0.16	0.27	0.16	−0.61	0.22
0.86	−0.87	0.08	−0.59	0.16	−0.43	0.17	−0.47	0.17	−0.28	0.29
0.90	−0.95	0.07	−0.87	0.11	−0.79	0.15	−0.61	0.15	−0.65	0.25
0.94	−0.93	0.06	−0.76	0.11	−0.61	0.10	−0.41	0.11	−0.42	0.21
0.97	−0.81	0.08	−0.72	0.15	−0.26	0.10	−0.23	0.11	−0.01	0.17

TABLE 4 (continued)

$\cos\theta^*$	1416 MeV/c		1449 MeV/c		1467 MeV/c		1500 MeV/c		1550 MeV/c	
	A_{0N}	±	A_{0N}	±	A_{0N}	±	A_{0N}	±	A_{0N}	±
−0.97	−0.90	0.89	−0.20	0.43	−0.82	0.57	−1.25	0.75	−0.07	0.36
−0.94	−0.37	0.43	−1.45	0.56	0.33	1.02	−0.10	0.37	−0.79	0.53
−0.90	−0.32	0.44	0.65	1.04	0.55	0.42	0.36	0.29	−0.49	0.46
−0.86	0.43	0.23	0.26	0.51	0.57	0.29	0.44	0.19	0.28	0.28
−0.82	0.55	0.14	1.04	0.15	0.99	0.15	0.73	0.18	0.96	0.21
−0.78	0.81	0.13	0.39	0.24	0.68	0.21	0.70	0.17	0.61	0.21
−0.74	0.75	0.10	0.75	0.18	1.00	0.14	0.86	0.17	0.75	0.20
−0.70	0.84	0.09	0.56	0.22	1.01	0.12	0.77	0.15	1.14	0.12
−0.66	0.87	0.11	0.57	0.20	0.85	0.15	0.70	0.17	0.97	0.16
−0.62	0.94	0.09	0.82	0.23	1.00	0.14	0.84	0.14	0.98	0.17
−0.58	0.96	0.10	0.69	0.24	0.96	0.16	0.53	0.17	0.87	0.21
−0.54	0.67	0.15	0.53	0.29	0.74	0.21	0.87	0.15	1.00	0.18
−0.50	0.78	0.14	0.88	0.25	0.57	0.21	0.62	0.22	0.69	0.34
−0.46	0.47	0.16	0.63	0.61	0.05	0.30	0.52	0.22	−0.30	0.95
−0.42	0.13	0.19	0.00	0.00	0.32	0.20	0.38	0.22	−1.37	2.21
−0.38	0.34	0.19	1.36	2.30	−0.09	0.27	0.06	0.24	0.65	0.45
−0.34	−0.06	0.20	−0.65	0.53	−0.20	0.23	−0.16	0.19	0.61	0.26
−0.30	−0.43	0.21	−0.13	0.34	0.42	0.32	−0.20	0.20	0.13	0.24
−0.26	0.11	0.21	−0.25	0.35	0.09	0.24	−0.28	0.18	0.22	0.23
−0.22	0.07	0.20	−0.27	0.25	−0.48	0.24	0.24	0.17	0.40	0.18
−0.18	0.51	0.18	0.46	0.31	0.45	0.22	0.43	0.13	−0.04	0.20
−0.14	0.27	0.15	0.89	0.22	0.51	0.14	0.37	0.15	0.05	0.25
−0.10	0.26	0.17	0.54	0.23	0.59	0.15	0.46	0.15	0.49	0.14
−0.06	0.40	0.14	0.64	0.21	0.64	0.14	0.45	0.13	0.46	0.18
−0.02	0.39	0.13	0.65	0.25	0.71	0.12	0.42	0.13	0.82	0.13
0.02	0.64	0.10	0.64	0.24	0.66	0.12	0.47	0.12	0.54	0.15
0.06	0.69	0.10	0.44	0.23	0.55	0.13	0.92	0.09	0.49	0.17
0.10	0.86	0.10	1.20	0.16	0.58	0.13	0.59	0.12	0.60	0.16
0.14	0.78	0.11	0.65	0.21	1.02	0.10	0.76	0.12	0.64	0.14
0.18	0.74	0.12	0.63	0.21	0.96	0.15	0.77	0.12	0.53	0.18
0.22	0.85	0.15	0.74	0.23	1.02	0.13	0.66	0.16	0.98	0.16
0.26	0.93	0.14	0.84	0.30	1.12	0.14	0.65	0.17	0.81	0.20
0.30	0.87	0.21	1.22	0.22	0.99	0.17	0.68	0.20	0.70	0.22
0.34	1.24	0.10	0.80	0.24	1.27	0.19	0.64	0.25	0.78	0.34
0.38	0.85	0.20	1.42	0.42	0.97	0.22	0.59	0.37	1.38	0.13
0.42	0.92	0.22	1.13	0.41	0.90	0.23	0.88	0.20	0.51	0.37
0.46	1.05	0.19	0.09	0.67	0.90	0.26	0.97	0.17	0.82	0.40
0.50	0.27	0.28	1.41	4.09	0.98	0.26	1.00	0.17	−0.01	0.66
0.54	0.79	0.20	1.42	1.84	0.91	0.20	0.72	0.21	0.00	0.00
0.58	0.96	0.19	1.41	0.29	0.25	0.34	0.56	0.23	0.97	0.19
0.62	0.72	0.16	1.24	0.18	0.89	0.18	0.52	0.29	0.55	0.25
0.66	0.97	0.19	1.23	0.32	1.05	0.23	0.74	0.24	0.87	0.23
0.70	0.73	0.19	0.42	0.33	0.76	0.21	0.64	0.28	0.92	0.18
0.74	0.52	0.19	0.60	0.66	1.09	0.19	0.57	0.23	0.54	0.32
0.78	0.59	0.24	0.48	0.58	0.78	0.28	0.90	0.19	0.60	0.36
0.82	0.44	0.24	−0.31	0.40	0.17	0.51	0.05	0.35	0.57	0.32
0.86	−0.07	0.23	−0.02	0.49	0.91	0.54	0.14	0.56	−0.59	0.60
0.90	−0.48	0.26	−0.82	0.36	−0.61	0.46	0.18	0.75	−0.64	0.53
0.94	−0.28	0.16	−0.02	0.29	0.03	0.26	−0.08	0.24	0.35	0.27
0.97	−0.20	0.12	0.20	0.24	0.32	0.19	0.98	0.15	0.36	0.18

and Morgan [8] remarked that in fitting earlier data they found it difficult to avoid large numbers of coherent resonant states. Thirdly, the 90° phase differences may well arise from alternating-*J* states on Regge trajectories, i.e. the staggering of

TABLE 5
Differential cross sections for p̄p → K⁻K⁻

cos θ*	360 MeV/c		404 MeV/c		467 MeV/c		497 MeV/c		523 MeV/c	
	$d\sigma/d\Omega$ [μb/sr]	±	$d\sigma/d\Omega$ [μb/sr]	±	$d\sigma/d\Omega$ [μb/sr]	±	$d\sigma/d\Omega$ [μb/sr]	±	$d\sigma/d\Omega$ [μb/sr]	±
−0.94	29.86	4.24	28.31	4.50	47.30	4.54	43.34	3.71	38.04	4.69
−0.85	20.11	3.13	18.81	5.19	36.85	4.65	35.17	3.66	29.56	2.74
−0.75	16.61	2.92	12.05	2.51	26.87	4.12	11.78	3.15	17.59	2.15
−0.65	10.68	6.27	12.13	4.88	20.65	8.99	17.38	9.46	9.67	2.28
−0.55	11.92	7.82	20.28	11.47	9.99	3.94	7.50	5.25	8.50	2.78
−0.45	10.78	4.56	20.14	12.30	8.31	4.06	6.51	3.91	6.39	1.77
−0.35	10.06	5.77	8.73	10.50	6.92	4.53	7.48	6.98	3.44	2.02
−0.25	20.86	4.59	25.27	9.26	19.20	6.65	11.40	3.34	9.89	2.21
−0.15	25.48	7.54	26.15	11.96	8.14	3.80	12.32	4.34	6.46	1.99
−0.05	16.68	6.25	5.85	7.62	4.25	4.66	20.18	7.99	8.99	2.94
0.05	22.80	4.36	10.38	6.55	3.89	5.03	10.04	2.12	9.67	5.19
0.15	25.46	7.47	13.13	3.66	15.12	7.58	8.08	2.47	11.21	8.66
0.25	15.18	6.55	9.83	4.78	7.59	4.61	6.99	5.37	9.07	2.77
0.35	20.54	6.71	12.56	8.86	11.14	3.19	6.37	2.51	5.60	1.82
0.45	18.20	8.52	16.73	7.48	11.48	4.38	8.32	3.56	4.70	1.85
0.55	12.01	4.93	8.15	5.61	12.23	3.22	6.24	2.44	8.46	2.00
0.65	16.52	5.05	7.39	3.55	12.46	3.54	12.50	2.75	9.09	1.92
0.75	9.04	3.38	12.78	3.89	12.48	2.81	12.74	3.20	14.22	2.12
0.85	12.07	8.12	18.65	7.33	9.36	5.18	15.66	7.54	17.43	2.72
0.94	24.46	3.09	25.72	8.08	28.69	2.48	39.87	3.76	24.59	4.54

cos θ*	585 MeV/c		679 MeV/c		783 MeV/c		886 MeV/c		988 MeV/c	
−0.94	37.79	3.98	41.84	3.39	37.75	2.08	33.23	2.15	23.04	2.11
−0.85	31.86	5.07	36.10	3.21	26.97	2.94	18.16	2.63	14.16	1.63
−0.75	16.52	2.39	18.04	2.15	11.46	1.40	12.98	1.72	3.58	0.86
−0.65	6.18	2.97	8.80	2.01	4.04	1.25	6.95	2.59	2.42	1.04
−0.55	6.24	5.96	5.42	3.57	3.20	1.08	3.95	1.25	3.82	1.02
−0.45	2.50	1.15	5.46	1.78	4.57	1.10	4.42	1.12	4.62	0.88
−0.35	1.40	1.31	4.49	1.91	2.38	0.81	3.68	1.11	3.59	0.68
−0.25	3.42	1.72	5.12	1.50	3.14	0.92	4.31	1.18	4.52	0.75
−0.15	6.48	2.43	5.94	1.37	3.10	0.81	6.21	1.30	3.64	0.58
−0.05	5.77	2.95	5.96	1.32	5.18	1.50	4.55	0.90	3.30	0.64
0.05	6.57	2.54	11.72	2.72	4.75	0.94	3.91	0.79	5.48	1.09
0.15	6.10	1.82	5.55	1.46	4.01	0.91	6.59	1.59	4.59	0.76
0.25	5.67	3.56	4.17	2.45	7.04	2.21	3.99	1.03	4.57	0.82
0.35	5.81	2.28	5.01	1.35	5.12	1.13	5.52	1.09	4.93	0.90
0.45	5.19	2.45	13.60	2.64	7.46	1.40	6.99	1.26	6.22	0.95
0.55	8.11	1.95	9.00	1.61	7.07	1.15	8.97	1.90	7.20	1.07
0.65	10.42	2.11	10.68	1.81	11.95	1.57	12.12	1.49	6.69	0.91
0.75	15.20	2.20	14.69	1.96	20.77	2.67	8.77	1.20	5.89	0.98
0.85	13.74	2.80	22.57	2.52	14.24	1.78	14.21	1.71	7.41	1.14
0.94	29.60	4.52	32.41	3.30	36.03	2.58	21.91	2.07	21.16	1.84

TABLE 5 (continued)

cos θ^*	1089 MeV/c		1190 MeV/c		1291 MeV/c		1351 MeV/c		1400 MeV/c	
	dσ/dΩ [μb/sr]	±	dσ/dΩ [μb/sr]	±	dσ/dΩ [μb/sr]	±	dσ/dΩ [μb/sr]	±	dσ/dΩ [μb/sr]	±
−0.94	22.25	2.73	18.58	2.60	7.23	1.82	7.33	1.54	8.25	2.43
−0.85	13.40	1.61	9.45	3.31	3.90	1.26	3.14	1.11	4.77	1.96
−0.75	4.60	0.95	3.44	1.54	3.35	1.20	2.02	1.03	2.36	1.14
−0.65	4.17	1.24	5.16	2.50	5.06	1.42	3.82	0.92	2.86	1.14
−0.55	4.76	1.18	3.30	1.51	4.29	1.05	3.29	0.69	2.96	1.16
−0.45	4.68	0.87	6.63	1.66	3.74	0.67	3.53	0.67	3.25	1.92
−0.35	4.12	0.74	5.00	1.05	3.26	0.59	3.36	0.62	3.58	1.29
−0.25	3.13	0.78	6.09	2.24	3.75	1.04	2.90	0.76	4.46	1.38
−0.15	3.72	0.60	4.61	1.42	3.75	0.75	2.91	0.71	8.15	3.51
−0.05	3.13	0.56	4.73	1.22	3.66	0.72	3.57	0.63	5.14	1.48
0.05	4.07	0.72	5.50	1.14	4.62	0.94	2.68	0.57	5.86	1.36
0.15	3.32	0.60	5.87	1.23	3.64	0.61	2.62	0.68	3.57	0.78
0.25	4.31	0.72	6.39	2.21	3.22	0.75	2.88	0.66	3.78	1.67
0.35	4.88	0.90	3.58	1.25	3.09	0.76	1.93	0.56	3.62	1.16
0.45	3.89	0.70	4.48	1.29	2.70	0.81	2.90	1.33	2.29	2.53
0.55	3.12	0.68	2.86	2.24	2.33	0.66	1.80	0.64	1.87	6.41
0.65	3.73	1.70	3.08	1.67	1.89	0.63	1.69	0.51	1.41	2.48
0.75	3.84	0.86	2.11	1.40	4.01	2.76	2.77	0.61	3.71	1.17
0.85	5.45	1.07	4.98	1.71	6.83	1.22	8.27	1.19	8.62	1.60
0.94	23.14	1.80	15.20	2.37	16.59	1.87	21.12	2.34	16.88	3.16

cos θ^*	1416 MeV/c		1449 MeV/c		1467 MeV/c		1500 MeV/c		1550 MeV/c	
−0.94	6.70	1.66	4.62	2.40	5.12	1.95	2.30	1.70	2.07	3.21
−0.85	4.95	1.03	4.24	3.75	5.24	1.00	4.35	1.34	3.56	1.45
−0.75	2.57	0.93	4.36	2.24	4.04	1.04	1.35	0.85	1.08	0.99
−0.65	3.95	1.08	3.59	1.94	5.05	1.21	2.71	0.84	3.75	2.13
−0.55	5.14	0.98	3.17	1.70	2.45	0.72	3.73	1.00	1.86	1.81
−0.45	4.43	0.98	4.27	2.30	3.46	0.94	3.88	1.13	1.24	2.43
−0.35	4.54	0.91	3.00	1.36	2.73	0.80	2.05	0.72	2.20	1.11
−0.25	2.69	0.81	5.26	1.92	2.97	0.77	2.66	0.85	2.00	1.26
−0.15	3.58	0.86	8.03	4.30	3.92	0.96	1.75	0.84	1.77	0.78
−0.05	4.12	0.90	9.64	3.05	4.14	0.91	4.27	1.16	3.59	1.42
0.05	4.34	0.84	7.12	2.58	2.15	1.26	2.58	0.76	3.55	1.17
0.15	4.15	1.05	3.70	1.87	2.74	1.11	3.48	0.89	3.55	1.17
0.25	3.95	1.24	7.03	3.36	3.04	1.58	1.83	0.70	1.47	0.70
0.35	2.13	0.85	3.12	2.79	1.86	1.36	2.32	0.62	2.46	1.92
0.45	3.58	1.17	2.30	4.74	1.81	0.91	2.73	3.78	3.31	2.41
0.55	2.65	1.01	0.00	0.00	2.74	0.96	1.69	0.93	1.44	2.54
0.65	2.78	1.13	2.44	1.56	3.94	0.96	2.45	0.95	3.81	1.44
0.75	3.99	0.88	3.93	2.10	3.44	0.84	3.09	0.92	4.54	1.34
0.85	7.68	1.16	11.32	3.21	8.27	1.48	8.30	2.61	8.75	1.93
0.94	13.55	1.87	16.05	4.09	18.17	1.92	14.79	1.83	13.04	1.74

$I = 0$ and $I = 1$ states. More definite conclusions must await detailed amplitude analyses.

Bardin et al. [21], in evaluating the electromagnetic form factor of the proton in

the time-like region, have normalised their results to integrated $\pi\pi$ and $\overline{K}K$ cross sections. We are in a position to re-evaluate these normalisations from our Legendre fits. Table 7 shows the results. They differ significantly from those used

TABLE 6

Asymmetries for $\bar{p}p \to K^-K^-$

cos θ^*	360 MeV/c		404 MeV/c		467 MeV/c		497 MeV/c		523 MeV/c	
	A_{0N}	±	A_{0N}	±	A_{0N}	±	A_{0N}	±	A_{0N}	±
−0.94	−0.40	0.12	−0.11	0.17	−0.16	0.10	0.17	0.07	0.27	0.27
−0.85	−0.61	0.09	−0.86	0.15	−0.36	0.14	−0.20	0.08	−0.27	0.20
−0.75	−0.76	0.19	−0.34	0.24	−0.44	0.30	−0.01	0.22	−0.39	0.21
−0.65	−1.40	0.23	−1.34	0.11	−0.89	0.39	−1.41	0.28	−0.67	0.20
−0.55	−0.38	0.43	−0.58	0.43	−1.00	0.28	−0.48	0.63	−1.05	0.23
−0.45	−1.02	0.37	−0.73	0.24	−0.58	0.39	−0.72	0.34	−0.90	0.19
−0.35	−0.96	0.43	−0.38	0.39	−0.15	0.47	0.01	0.62	0.48	0.41
−0.25	0.25	0.26	0.07	0.47	0.65	0.47	0.36	0.34	0.44	0.28
−0.15	−0.23	0.21	0.20	0.42	0.20	0.33	0.59	0.23	0.57	0.21
−0.05	−0.18	0.17	0.15	0.48	−0.38	0.26	0.68	0.24	0.38	0.19
0.05	0.34	0.16	0.51	0.39	0.00	2.02	0.55	0.22	0.89	0.26
0.15	0.37	0.16	−0.27	0.25	−0.03	0.33	0.42	0.26	−0.24	0.49
0.25	0.20	0.45	0.18	0.49	0.73	0.46	0.51	0.58	0.67	0.23
0.35	0.16	0.36	0.34	0.36	0.35	0.27	0.41	0.29	0.33	0.24
0.45	−0.22	0.54	0.29	0.26	0.37	0.29	0.20	0.38	0.01	0.20
0.55	−0.25	0.37	−0.05	0.36	−0.38	0.25	0.13	0.31	−0.23	0.18
0.65	−0.25	0.35	0.40	0.24	0.20	0.17	−0.16	0.24	−0.25	0.15
0.75	−0.34	0.48	−0.27	0.31	−0.21	0.20	−0.52	0.30	−0.19	0.13
0.85	−0.24	0.21	−0.29	0.17	−0.03	0.14	−0.33	0.14	−0.32	0.09
0.94	0.30	0.27	0.07	0.16	−0.05	0.10	−0.14	0.11	−0.26	0.08
	585 MeV/c		679 MeV/c		783 MeV/c		886 MeV/c		988 MeV/c	
−0.94	0.28	0.23	0.06	0.12	−0.03	0.10	0.34	0.11	−0.01	0.11
−0.85	0.08	0.14	−0.15	0.14	0.23	0.13	0.47	0.13	0.87	0.48
−0.75	−0.61	0.14	0.03	0.12	0.19	0.16	0.38	0.16	0.67	0.25
−0.65	−0.84	0.29	−0.05	0.21	0.04	0.21	1.09	0.23	0.96	0.26
−0.55	−0.63	0.35	−0.46	0.23	0.72	0.27	1.06	0.16	0.86	0.21
−0.45	0.00	0.24	0.36	0.20	0.74	0.17	1.00	0.15	0.62	0.15
−0.35	0.13	0.42	1.01	0.24	0.43	0.24	0.43	0.20	0.47	0.15
−0.25	0.74	0.34	0.84	0.23	0.80	0.21	0.74	0.19	0.69	0.15
−0.15	0.45	0.23	0.56	0.18	0.46	0.15	0.78	0.12	0.54	0.14
−0.05	0.88	0.17	0.78	0.14	0.58	0.15	0.61	0.13	0.37	0.16
0.05	0.54	0.17	0.68	0.17	0.62	0.14	0.69	0.12	0.47	0.14
0.15	0.54	0.20	0.30	0.25	0.23	0.19	0.24	0.17	0.52	0.16
0.25	0.38	0.30	0.49	0.24	0.76	0.13	0.50	0.17	0.34	0.17
0.35	0.20	0.20	0.14	0.17	0.55	0.14	0.63	0.13	0.29	0.15
0.45	0.28	0.18	0.35	0.14	0.17	0.14	0.46	0.13	0.41	0.15
0.55	−0.01	0.13	0.02	0.13	0.18	0.12	0.40	0.12	0.55	0.13
0.65	−0.17	0.12	0.30	0.11	0.28	0.10	0.36	0.10	0.24	0.14
0.75	−0.09	0.11	−0.12	0.10	0.19	0.10	0.37	0.11	0.09	0.15
0.85	−0.13	0.10	−0.07	0.08	0.28	0.08	0.02	0.09	−0.06	0.12
0.94	−0.13	0.08	0.05	0.07	0.04	0.07	0.07	0.08	−0.06	0.09

TABLE 6 (continued)

cos θ^*	1089 MeV/c		1190 MeV/c		1291 MeV/c		1351 MeV/c		1400 MeV/c	
	A_{0N}	±	A_{0N}	±	A_{0N}	±	A_{0N}	±	A_{0N}	±
−0.94	0.10	0.18	0.77	0.34	−0.15	0.40	0.25	0.16	0.35	0.75
−0.85	0.85	0.24	0.78	0.95	−0.34	0.54	0.34	0.22	−0.17	1.17
−0.75	1.11	0.20	0.75	0.33	1.15	0.31	1.09	0.28	0.99	0.47
−0.65	1.03	0.13	1.00	0.29	0.82	0.14	0.94	0.16	0.80	0.26
−0.55	1.13	0.11	0.41	0.27	0.72	0.15	0.76	0.13	0.89	0.26
−0.45	0.87	0.13	0.83	0.17	0.85	0.12	0.70	0.15	0.21	1.65
−0.35	0.96	0.12	0.83	0.16	0.93	0.10	0.82	0.16	0.81	0.19
−0.25	0.84	0.12	0.86	0.24	0.63	0.13	0.79	0.18	0.81	0.20
−0.15	0.72	0.13	0.94	0.23	0.69	0.12	0.91	0.18	0.87	0.21
−0.05	0.69	0.15	0.86	0.19	0.82	0.12	0.96	0.13	0.45	0.21
0.05	1.00	0.09	0.80	0.17	0.75	0.10	0.93	0.12	0.75	0.18
0.15	1.05	0.12	0.84	0.17	0.73	0.11	1.00	0.13	1.01	0.17
0.25	0.81	0.15	1.02	0.29	1.01	0.09	0.98	0.13	0.93	0.26
0.35	1.02	0.14	0.79	0.22	0.96	0.14	0.84	0.17	0.61	0.30
0.45	0.97	0.15	0.96	0.19	1.04	0.17	0.95	0.15	1.09	0.64
0.55	1.05	0.13	0.89	0.26	0.69	0.20	0.35	0.24	−0.89	1.19
0.65	1.02	0.16	0.76	0.22	0.44	0.21	0.33	0.23	1.11	0.49
0.75	0.63	0.19	0.74	0.33	1.12	0.16	1.14	0.13	0.95	0.30
0.85	0.34	0.15	0.25	0.21	0.54	0.15	0.62	0.12	0.87	0.14
0.94	−0.03	0.08	0.13	0.15	0.50	0.10	0.48	0.08	0.59	0.13

	1416 MeV/c		1449 MeV/c		1467 MeV/c		1500 MeV/c		1550 MeV/c	
−0.94	0.04	0.29	0.51	0.65	1.13	1.15	−1.00	1.34	1.41	0.57
−0.85	1.11	0.64	0.32	0.92	−0.19	0.56	0.66	0.82	−0.24	0.68
−0.75	1.00	0.26	1.21	0.30	0.90	0.25	0.68	0.56	0.84	0.38
−0.65	1.10	0.20	−0.01	0.59	1.24	0.24	0.53	0.29	0.29	0.34
−0.55	0.59	0.15	1.36	0.28	0.87	0.28	0.65	0.23	1.15	0.68
−0.45	0.93	0.13	−0.51	1.34	0.81	0.24	0.68	0.20	1.37	0.81
−0.35	0.87	0.16	1.08	0.28	0.62	0.30	0.78	0.17	0.70	0.25
−0.25	0.78	0.19	0.97	0.40	0.81	0.24	0.66	0.21	0.24	0.33
−0.15	0.99	0.18	1.01	0.31	0.82	0.25	0.95	0.14	0.48	0.30
−0.05	0.82	0.19	1.12	0.17	0.62	0.24	0.48	0.22	0.66	0.32
0.05	0.63	0.14	0.72	0.24	0.60	0.20	0.76	0.15	0.40	0.27
0.15	0.95	0.13	0.92	0.38	0.57	0.20	0.50	0.17	0.70	0.20
0.25	0.79	0.18	0.68	0.40	1.21	0.19	0.76	0.22	1.05	0.33
0.35	0.73	0.23	1.03	0.59	0.63	0.25	0.86	0.23	1.38	0.27
0.45	0.82	0.29	1.01	0.73	0.64	0.30	0.16	0.51	0.47	0.62
0.55	0.52	0.37	0.00	0.00	0.89	0.27	0.97	0.22	0.89	1.10
0.65	0.89	0.22	1.41	0.46	0.70	0.20	−0.02	0.37	1.03	0.35
0.75	0.86	0.18	1.43	0.19	0.67	0.19	0.79	0.15	0.44	0.23
0.85	0.81	0.12	0.78	0.22	0.61	0.16	0.60	0.12	0.42	0.19
0.94	0.51	0.09	0.71	0.19	0.38	0.11	0.06	0.12	0.17	0.17

by Bardin et al. and change their results by amounts well beyond their errors. Presumably, this arises from discrepancies in normalisation between the data of Tanimori et al. and Eisenhandler et al. The result is to increase the value of G^p at 540 MeV/c and decrease it at 900 MeV/c, bringing the results on to a much
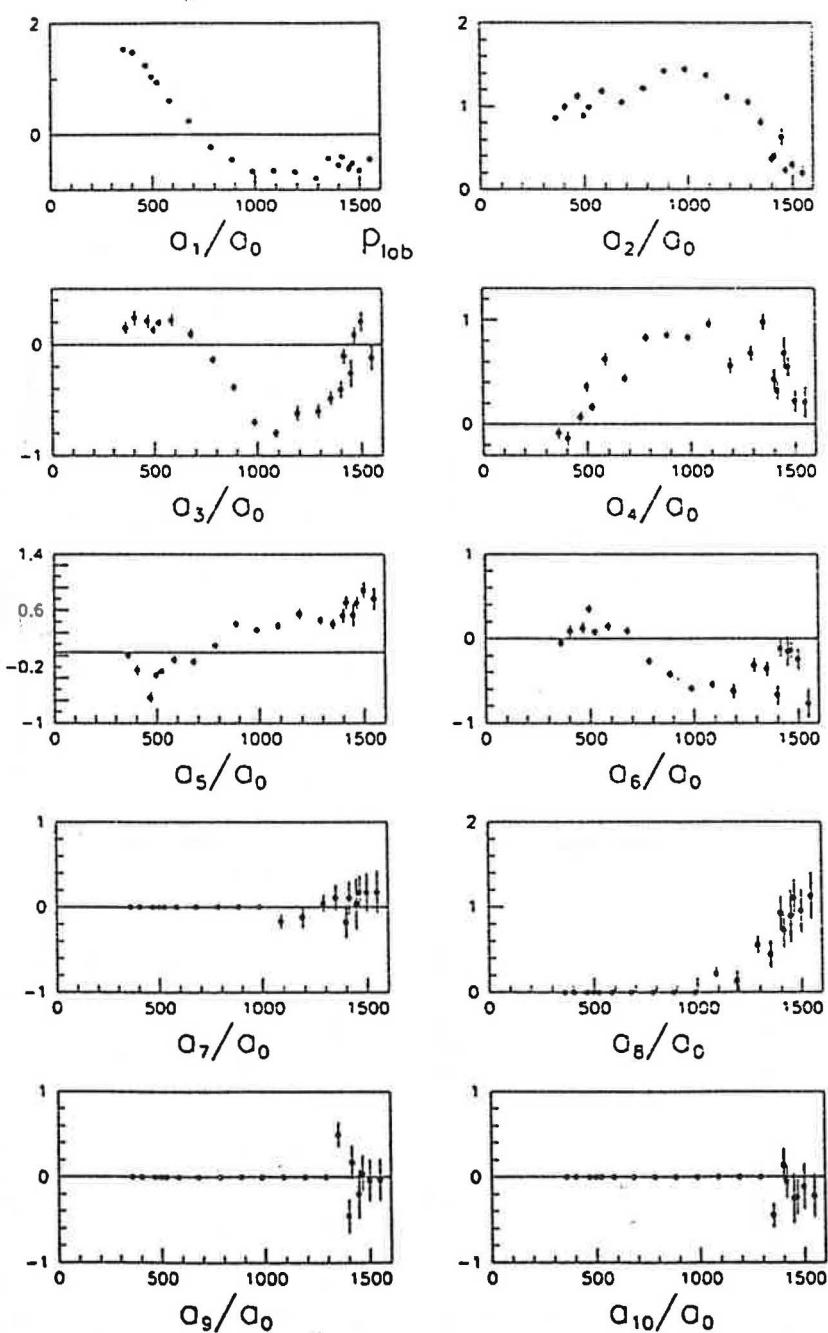
Fig. 22. Legendre coefficients for $d\sigma/d\Omega(\bar{p}p \to \pi^-\pi^+)$, normalised to a_0.
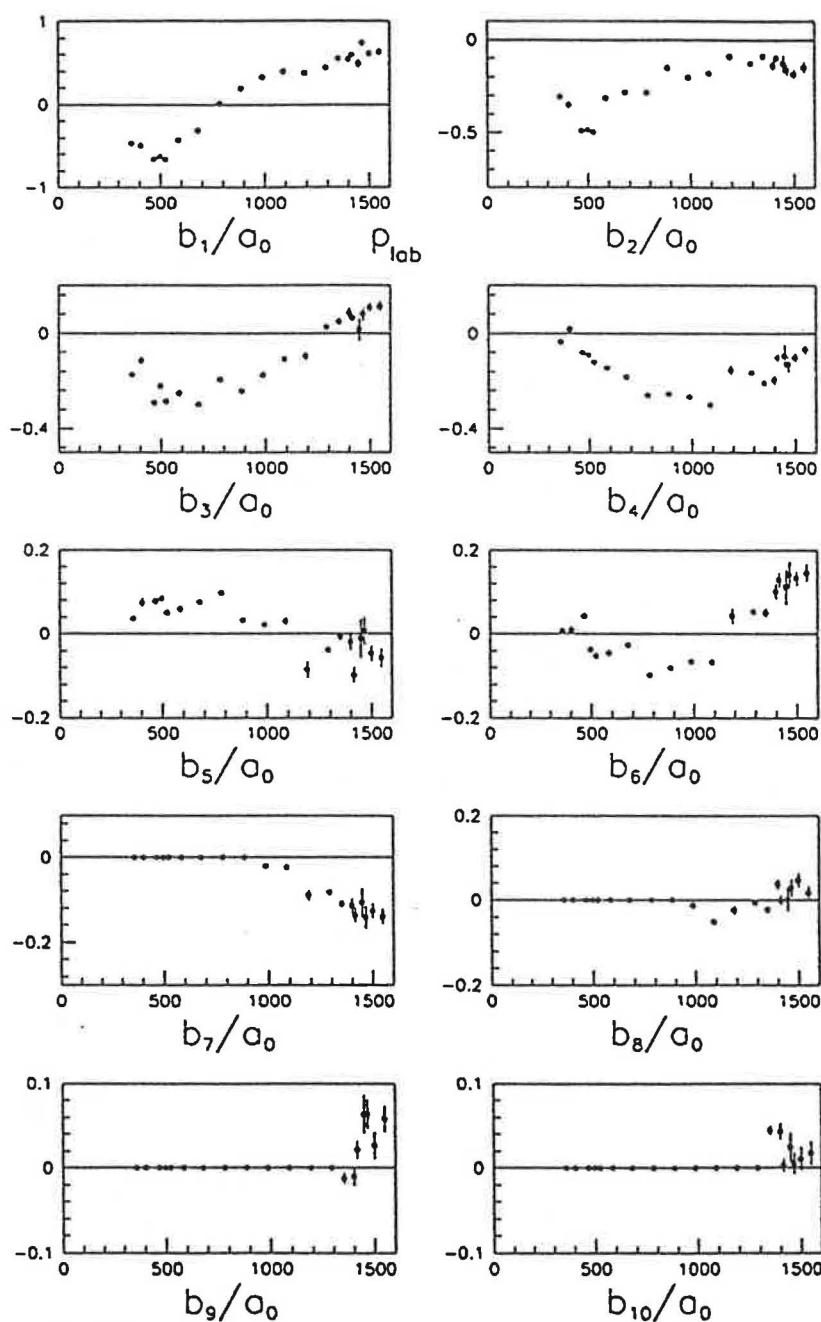
Fig. 23. Legendre coefficients for $A_{0N}\, d\sigma/d\Omega(\bar{p}p \to \pi^-\pi^+)$, normalised to a_0.
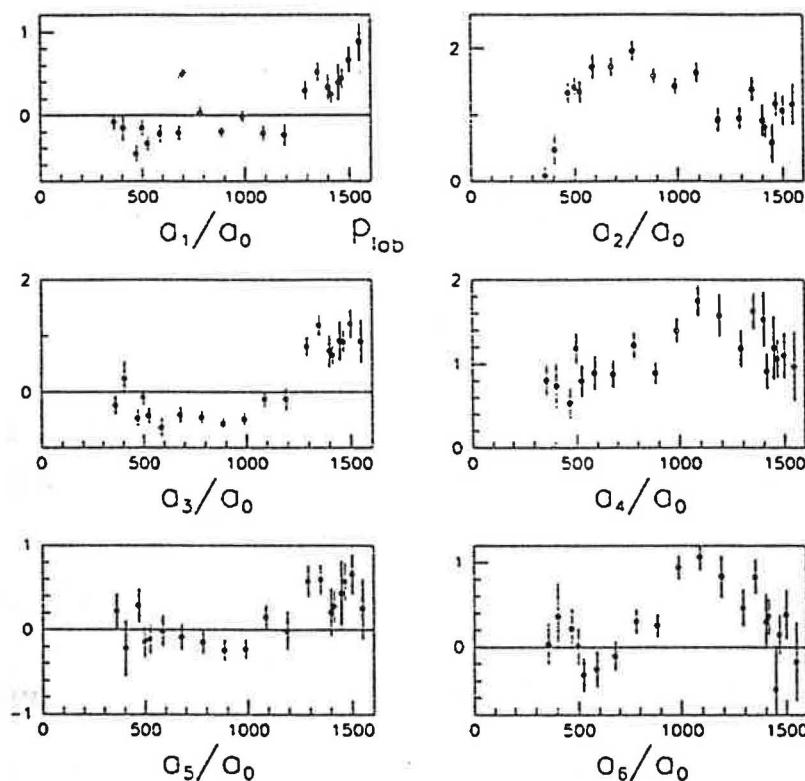
Fig. 24. Legendre coefficients for $d\sigma/d\Omega(\bar{p}p \rightarrow K^-K^-)$, normalised to a_0.

TABLE 7

Differential cross sections integrated (a) from $\cos\theta = -0.8$ to $+0.8$, (b) from -0.7 to 0.9 for $\pi\pi$ and $\bar{K}K$ final states

Momentum [MeV/c]	(a)		(b)	
	$\pi\pi$ [μb]	$\bar{K}K$ [μb]	$\pi\pi$ [μb]	$\bar{K}K$ [μb]
360	430	164		
404	360	130		
467	371	112		
497	354	98		
523	354	87		
585	305	69		
679	310	82		
783	269	59	265	65
886	224	62	214	64
988	175	46	161	49
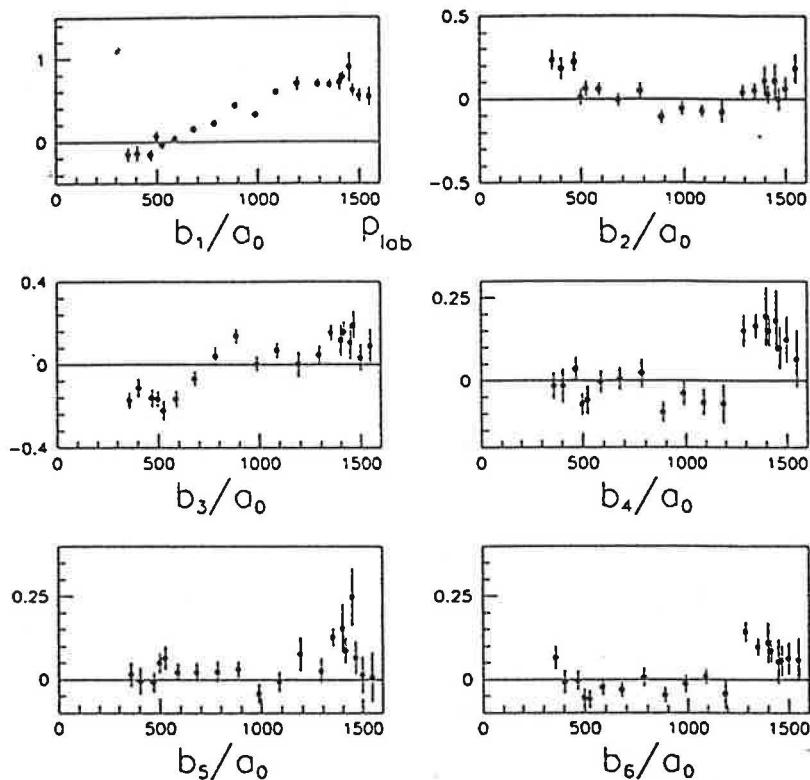
Fig. 25. Legendre coefficients for $A_{0N} \, d\sigma/d\Omega(\bar{p}p \to K^-K^-)$, normalised to a_0.

smoother curve than before. However, we caution that one should still assign a normalisation uncertainty of $\pm 10\%$ to integrated $\pi\pi$ and $\overline{K}K$ cross sections, hence a systematic normalisation uncertainty on G^P of $\pm 5\%$ over the range 540–900 MeV/c.

References

[1] M.A. Mandelkern et al., Phys. Rev. D4 (1971) 2658
[2] R.D. Ehrlich et al., Phys. Rev. Lett. 28 (1972) 1147
[3] E. Eisenhandler et al., Nucl. Phys. B96 (1975) 109

[4] A.A. Carter et al., Nucl. Phys. B127 (1977) 202
[5] A.A. Carter et al., Phys. Lett. B67 (1977) 117
[6] R.S. Dulude et al., Phys. Lett. B79 (1978) 329; 335
[7] A.D. Martin and M.R. Pennington, Nucl. Phys. B169 (1980) 216
[8] B.R. Martin and D. Morgan, Nucl. Phys. B176 (1980) 355
[9] B.R. Martin and G.C. Oades, Nucl. Phys. A483 (1988) 669
[10] D.V. Bugg, Phys. Lett. B52 (1974) 102
[11] T. Tanimori et al., Phys. Rev. D41 (1990) 744
[12] T. Tanimori et al., Phys. Rev. Lett. 55 (1985) 1835
[13] F. Sai, S. Sakamoto and S.S. Yamamoto, Nucl. Phys. B213 (1983) 371
[14] G. Bardin et al., Phys. Lett. B255 (1991) 149
[15] R.M. Baltrusaitis et al., Phys. Rev. Lett. 56 (1986) 107
[16] J. Sculli et al., Phys. Rev. Lett. 58 (1987) 1715
[17] F. Tessarotto et al., Nucl. Phys. Suppl. B8 (1989) 141
[18] R.A. Kunne et al., Nucl. Phys. B323 (1989) 1
[19] R.A. Kunne, Ph.D. thesis, University of Amsterdam (1988)
[20] A. Hasan, Ph.D. thesis, University of London (1991)
[21] G. Bardin et al., CERN preprint PPE/91-30